

1 **An evaluation of the ocean and sea ice climate of E3SM**
2 **using MPAS and interannual CORE-II forcing**

3 **Mark R. Petersen^{1*}, Xylar S. Asay-Davis², Anne S. Berres³, Qingshan Chen⁴,**
4 **Nils Feige³, Matthew J. Hoffman², Douglas W. Jacobsen², Philip W. Jones²,**
5 **Mathew E. Maltrud², Stephen F. Price², Todd D. Ringler², Gregory J. Strelitz^{3,5},**
6 **Adrian K. Turner², Luke P. Van Roekel², Milena Veneziani², Jonathan D. Wolfe²,**
7 **Phillip J. Wolfram², Jonathan L. Woodring³**

8 ¹ Computational Physics and Methods (CCS-2), Los Alamos National Laboratory, Los Alamos, NM, USA

9 ² Fluid Dynamics and Solid Mechanics (T-3), Los Alamos National Laboratory, Los Alamos, NM, USA

10 ³ Applied Computer Science (CCS-7), Los Alamos National Laboratory, Los Alamos, NM, USA

11 ⁴ Clemson University Mathematical Sciences Department, Clemson, NC, USA

12 ⁵ Department of Computer Science, University of California, Davis, CA, USA

13 **Key Points:**

- 14 • The Energy Exascale Earth System Model (E3SM) is a new climate model by the
15 US Department of Energy
16 • E3SM ocean and ice components use unstructured horizontal meshes for variable
17 resolution simulations
18 • 310-year E3SM simulations agree well with observed sea surface temperature,
19 mixed layer depths and sea ice coverage.

*

Corresponding author: Mark R. Petersen, mpetersen@lanl.gov

Abstract

The Energy Exascale Earth System Model (E3SM) is a new coupled Earth system model sponsored by the US Department of Energy. Here we present E3SM global simulations using active ocean and sea ice that are driven by the CORE-II inter-annual atmospheric forcing data set. The E3SM ocean and sea-ice components are MPAS-Ocean and MPAS-Seaice, which use the Model for Prediction Across Scales (MPAS) framework and run on unstructured horizontal meshes. For this study, grid cells vary from 30 to 60 km for the low resolution mesh and 6 to 18 km at high resolution. The vertical grid is a structured z-star coordinate and uses 60 and 80 layers for low and high resolution, respectively. The lower resolution simulation was run for five CORE cycles (310 years) with little drift in sea surface temperature or heat content. The meridional heat transport is within observational range, while the meridional overturning circulation at 26.5°N is low compared to observations. The largest temperature biases occur in the Labrador Sea and western boundary currents, and the mixed layer is deeper than observations at northern high latitudes in the winter months. In the Antarctic, maximum mixed layer depths (MLD) compare well with observations, but the spatial MLD pattern is shifted relative to observations. Sea-ice extent, volume and concentration agree well with observations. At high resolution, the sea surface height compares well with satellite observations in mean and variability.

1 Introduction

The purpose of this manuscript is to introduce a new global coupled climate model, the Energy Exascale Earth System Model (E3SM), to the research community by describing ocean-sea ice simulations forced by a data atmosphere. E3SM is the first climate model where all components are capable of regional refinement of the horizontal grid. This new capability allows researchers to place high resolution where it is most beneficial for the topic at hand, be it regional climate studies, coastal impacts, or melting under ice shelves.

Several advancements were required for a variable-resolution climate model to come to fruition. In the ocean, a critical step was the discretization of the primitive equations on unstructured meshes that conserves mass, energy, and potential vorticity in the same way as the continuous equations [Thuburn *et al.*, 2009; Ringler *et al.*, 2010]. This new ocean formulation is on an Arakawa “C-grid” [Arakawa and Lamb, 1977] with normal vectors on edges, rather than the “B-grid” with full vectors on vertices as used by the Parallel Ocean Program [POP; Smith *et al.*, 2010]. For the sea-ice model, the variational divergence of stress operator of Hunke and Dukowicz [2002] was adapted to the Voronoi cells of MPAS meshes, from the quadrilateral cells used by the Los Alamos sea ice model (CICE). An unstructured mesh requires a completely new array structure, as horizontal neighbors are defined by new pointer variables rather than the next i or j index, as in structured-mesh codes. The added complexity of an unstructured mesh extends to other parts of the code, including halos for message passing, higher order stencils, tensor operations, and interpolation.

These fundamental changes motivated the development of a completely new code base, the Model for Prediction Across Scales (MPAS), which is an unstructured-mesh framework for climate model components. E3SM includes MPAS components for ocean, sea ice, and land ice. The E3SM Atmosphere Model (EAM) uses the High Order Method Modelling Environment (HOMME) spectral element dynamical core [Evans *et al.*, 2013], which also supports regionally-refined grids. The transition to unstructured meshes also required the development of new tools for analysis, initial condition generation, and coupling. This undertaking, by the U.S. Department of Energy and collaborators, began with the creation of individual components from 2010 to 2014 [Ringler *et al.*, 2013; Petersen

70 *et al.*, 2015], and then coupling and simulations within the new E3SM (formerly named
71 the Accelerated Climate Model for Energy, ACME).

72 So was it worth it? After decades of development, global climate models on struc-
73 tured grids are highly refined for both physical fidelity and computational performance,
74 and set a high bar for success for a new Earth System Model (ESM). Yet, given successes
75 at the global scale, combined with advances in computing power, there is now a transition
76 from questions about *global mean* changes, embodied by the first five reports by the In-
77 tergovernmental Panel on Climate Change (IPCC) [Stocker *et al.*, 2013], to impact assess-
78 ment at regional and decadal scales. Unstructured meshes bring significant new potential
79 to enable regionally-refined simulations in ESMs given the lower computational cost rela-
80 tive to global high-resolution. Quantifying regional alterations in climate processes and
81 future impacts requires both high resolution and ensembles of simulations, making the
82 computational efficiency gained by placing the majority of grid cells in regions of interest
83 highly desirable. The investment in E3SM has produced new methods and codes in order
84 to enable this new capability for scientific inquiry and risk assessment. This paper is a
85 first step in evaluating the new model.

86 Here we present standard “CORE-forced” simulations, which have active ocean
87 and sea ice components, but data atmospheric forcing and run-off from the Coordinated
88 Ocean-ice Reference Experiments II (CORE-II) forcing dataset [Large and Yeager, 2009].
89 Validation and model intercomparisons are critical steps for any new climate model, and
90 the CORE-II standard offers a rich variety of literature to compare with other IPCC-class
91 models as well as observations over the reanalysis period (*e.g.* Danabasoglu *et al.* [2014a];
92 Griffies *et al.* [2014]; Downes *et al.* [2015]; Danabasoglu *et al.* [2016]). To evaluate the
93 multi-resolution capability of the E3SM ocean component, we present results from two
94 meshes: an eddy closure (EC) mesh that parameterizes mesoscale eddies; and a Rossby
95 Radius of deformation Scaling (RRS) mesh that resolves mesoscale eddies over most of
96 the globe. In these meshes, grid cell areas vary across the globe by a factor of two or
97 three. The purpose of this study is to demonstrate the capability of E3SM on relatively
98 uniform global meshes that are similar to previous studies with structured ocean model
99 grids. Simulations with more dramatic variations in resolution, like those in Sein *et al.*
100 [2017], will be explored in future work.

101 The manuscript is organized as follows. Section 2 describes model components, res-
102 olution, and forcing. Section 3 presents analysis from five CORE-cycles of a lower resolu-
103 tion simulation, plus 35 years of high-resolution results, and conclusions are presented in
104 Section 4.

105 **2 Model configuration**

106 All MPAS components share a common software framework for operations on the
107 unstructured horizontal mesh, which is based on Voronoi tessellations using a hexagonal
108 mesh. The MPAS framework is parallelized through the use of OpenMP, MPI, parallel-
109 netcdf, and PIO. Multiple hydrodynamic cores have been produced based on generalized
110 discretizations for the Voronoi tessellations [Thuburn *et al.*, 2009; Ringler *et al.*, 2010] and
111 include a shallow-water model [Ringler *et al.*, 2011], an ocean model [Ringler *et al.*, 2013],
112 a hydrostatic atmosphere [Rauscher *et al.*, 2012], a nonhydrostatic atmosphere [Skamarock
113 *et al.*, 2012], a sea ice model, and a land ice model [Hoffman *et al.*, 2018].

114 **2.1 Ocean component**

115 MPAS-Ocean is the ocean component of E3SM (version 1). MPAS-Ocean has been
116 previously validated as a stand-alone ocean model with global high-resolution and variable-
117 resolution simulations [Ringler *et al.*, 2013] and with standard idealized test cases [Pe-
118 tersen *et al.*, 2015; Reckinger *et al.*, 2015; Wolfram *et al.*, 2015; Ringler *et al.*, 2017]. It is a

finite volume discretization of the primitive equations and invokes the hydrostatic, incompressible, and Boussinesq approximations on a staggered C-grid.

Grid cells are typically near-hexagons (Fig. 2), but cells may have any number of sides; the algorithms and code are identical for all cell shapes. The horizontal discretization of the continuous equations was derived using mimetic methods and guarantees conservation of mass, potential vorticity and energy [Thuburn *et al.*, 2009; Ringler *et al.*, 2010], making it well-suited to the simulation of mesoscale eddies. The tracer advection scheme is the quasi 3rd-order flux corrected transport (FCT) scheme [Skamarock and Gassmann, 2011] with separate limiting in the horizontal and vertical. The MPAS-Ocean time stepping method is split-explicit, where the barotropic component is subcycled within each baroclinic time step.

The MPAS-Ocean vertical grid is structured and uses an arbitrary Eulerian-Lagrangian (ALE) method with several choices of vertical coordinates [Petersen *et al.*, 2015]. The simulations presented here use z-star, where the layer thicknesses of the full column expand and contract with the sea surface height [Adcroft and Campin, 2004]. The prognostic volume equation of state includes surface fluxes from the coupler, thus virtual salinity fluxes are not needed.

Vertical mixing is computed implicitly at the end of each time step, where the CVMix library¹ is called to compute the vertical diffusion and viscosity in each column using the K-profile parameterization (KPP, Large *et al.* [1994]). KPP itself has been implemented in numerous ocean circulation models. Each implementation makes slightly distinct physical and numerical choices. Sometimes, these implementation choices have unintended consequences that can negatively impact the KPP boundary layer simulation. These issues motivated the development of the CVMix library, which is a suite of standardized vertical mixing parameterizations for implementation in a three-dimensional ocean circulation model. Our configuration of KPP is based on the results of an intermodel comparison against large eddy simulations.

A mesoscale eddy parameterization is needed for the lower resolution mesh (EC60to30), so the current simulations employ the classic Gent and McWilliams [1990] eddy transport (GM) parameterization. The GM coefficient was tuned, in part, to help match observational estimates of transport through the Drake Passage, resulting in a value of $600 \text{ m}^2\text{s}^{-1}$ for the bolus component for the standard simulation. A full set of five core cycles was also run with a higher value of $1800 \text{ m}^2\text{s}^{-1}$, but resulted in very weak Southern Ocean transports and Atlantic overturning. Previous publications have explored alternative implementations of GM with spatially variable coefficients in idealized [Ringler and Gent, 2011; Chen *et al.*, 2016] and realistic domains [Gent and Danabasoglu, 2011], but a constant value was used here for simplicity and comparison with other CORE-forced studies [Griffies *et al.*, 2009; Danabasoglu *et al.*, 2014a]. The Redi component [Redi, 1982], which adds diffusion along isopycnal layers was set to zero for this set of simulations. In contrast to the EC60to30, the high-resolution RRS18to6 simulation directly resolves much of the mesoscale eddy activity and consequently the GM parameterization is not needed.

Initial conditions for temperature and salinity are interpolated from the Polar Science Center Hydrographic Climatology, version 3 [Steele *et al.*, 2001]. MPAS-Ocean has an “init mode” capability in the same executable as the forward model, which includes scalable file writing and interpolation tools to produce initial conditions. This is required at high resolution, where the file size of the ocean initial condition is 29 GB. The ocean is started from rest and spun up for several months, forced by an annual average wind stress and restoring of temperature and salinity at the top layer, in order to create an initial condition for E3SM.

¹ <https://github.com/CVMix/CVMix-src>, <https://doi.org/10.5281/zenodo.1000800>

168 Additional features that are available in MPAS-Ocean but not used in this study in-
 169 clude Lagrangian particles [Wolfram *et al.*, 2015; Wolfram and Ringler, 2017a,b], the abil-
 170 ity to run with sub-ice shelf ocean cavities in Antarctica [Asay-Davis *et al.*, 2017], and
 171 the computation of the Eliassen-Palm flux tensor to diagnose momentum transfer due to
 172 eddy-mean flow interactions [Saenz *et al.*, 2015; Ringler *et al.*, 2017]. MPAS-Ocean in-
 173 cludes a full biogeochemistry module based on the Biogeochemical Elemental Cycling
 174 (BEC) model developed for Community Earth System Model (CESM, Moore *et al.* [2004,
 175 2013]). In-situ model diagnostics are used throughout to demonstrate preparedness for
 176 next-generation exascale high performance computing [Woodring *et al.*, 2016].

177 2.2 Sea-ice component

178 The sea-ice component of E3SM is MPAS-Seaice. MPAS-Seaice solves the same
 179 sea-ice momentum equation and uses the same ‘B’ grid [Arakawa and Lamb, 1977] and
 180 Elastic-Viscous-Plastic (EVP) rheology [Hunke and Dukowicz, 1997] as the CICE sea-ice
 181 model [Hunke *et al.*, 2015], but with its divergence of internal stress operator adapted to
 182 work with the polygonal cells used by the MPAS framework, instead of the quadrilateral
 183 cells used by CICE. The divergence of stress operator uses an adaptation of the variational
 184 scheme from Hunke and Dukowicz [2002]. Instead of the bilinear basis functions used in
 185 Hunke and Dukowicz [2002], MPAS-Seaice uses Wachpress basis functions [Dasgupta,
 186 2003]. MPAS-Seaice uses an incremental remapping scheme, similar to that of Dukowicz
 187 and Baumgardner [2000], Lipscomb and Hunke [2004], and Lipscomb and Ringler [2005],
 188 to transport sea-ice concentration and tracers. The scheme of Lipscomb and Hunke [2004]
 189 was implemented for quadrilateral structured meshes and is used in CICE [Hunke *et al.*,
 190 2015]. The Lipscomb and Ringler [2005] scheme was implemented for a structured Spher-
 191 ical Centroidal Voronoi Tessellation mesh.

192 MPAS-Seaice uses the same column physics and biogeochemistry code as CICE. For
 193 simulations presented here, MPAS-Seaice used the “mushy layer” vertical thermodynamics
 194 of Turner *et al.* [2013]; Turner and Hunke [2015], the delta-Eddington shortwave radiation
 195 scheme of Briegleb and Light [2007]; Holland *et al.* [2012], a level-ice melt-pond scheme
 196 Hunke *et al.* [2013], the scheme for transport in thickness space of Lipscomb [2001] and
 197 representations of mechanical redistribution [Lipscomb *et al.*, 2007].

198 MPAS-Seaice is coupled to MPAS-Ocean in the same way as CICE is coupled to
 199 POP in the CESM [Craig *et al.*, 2012], except for several changes needed to accommodate
 200 differences in formulation between MPAS-Ocean and POP. First, MPAS-Ocean provides a
 201 mass of frazil ice formed, instead of the freezing potential to represent frazil ice formation
 202 provided by POP. MPAS-Seaice then converts the mass of frazil ice formed to a freez-
 203 ing potential. Second, since MPAS-Ocean’s free surface may be depressed to arbitrary
 204 depths, MPAS-Seaice provides the weight of sea-ice and snow to MPAS-Ocean. This al-
 205 lows MPAS-Ocean to compute the appropriate depression of the ocean surface due to this
 206 weight. The ocean model returns the sea surface gradient to the sea-ice model, which then
 207 calculates from it a surface tilt force. This sea surface gradient is relaxed to zero with a
 208 one day timescale to prevent a numerical coupling instability.

209 The CORE forced simulations were started with sea ice present above 70°N and be-
 210 low 60°S, with an initial ice concentration of one, a thickness of 1 m, and no snow. Ice
 211 salinity was set to the profile of Bitz and Lipscomb [1999], and the ice temperature profile
 212 was set as linear between the minimum of the ice melting temperature and the air temper-
 213 ature at the top surface and the ocean freezing temperature at the basal surface.

214 2.3 Atmospheric forcing

215 The CORE-II forcing data set [Griffies *et al.*, 2009; Large and Yeager, 2009] is the
 216 international standard for ocean-sea ice simulations within the World Climate Research

resolution	cell size		horiz. cells $\times 10^6$	vertical layers	compute Mcpu-hrs /century
	max km	min km			
low: EC60to30	60	30	0.23	60	0.36
high: RRS18to6	18	6	3.7	80	11.17

239 **Table 1.** Resolutions of MPAS-Ocean and MPAS-Sea Ice. The abbreviations correspond to the global
 240 mesh density function: EC is low resolution and requires a mesoscale Eddy Closure parameterization; grid-
 241 cell size (km) in RRS domain scales with the Rossby Radius of deformation in latitude. Compute time was
 242 measured on a cluster of Intel Xeon Broadwell nodes (see Sec. 2.5).

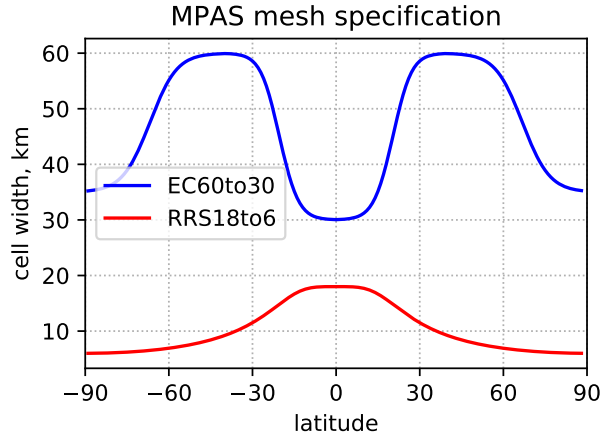
217 Programme (WCRP) Coupled Model Intercomparison Project (CMIP) and is based on
 218 the National Centers for Environmental Predictions (NCEP)/ National Center for Atmo-
 219 spheric Research (NCAR) atmospheric reanalysis with further corrections guided by obser-
 220 vations. The CORE-II data set is commonly used by different modeling centers to evaluate
 221 ocean model performance across physically realistic forcing scenarios (e.g., *Danabasoglu*
 222 *et al.* [2014a]; *Griffies et al.* [2014]; *Downes et al.* [2015]; *Danabasoglu et al.* [2016]) The
 223 CORE-II climate simulations are a benchmark that is well-suited to provide short-term,
 224 seasonal and yearly climatologies, allowing assessment of oceanic model dynamics within
 225 the context of other CMIP ocean models. In CMIP6 there will be an Ocean Model Inter-
 226 comparison Project (OMIP, *Griffies et al.* [2016]) as part of the CMIP6-MIPS, that will
 227 use the CORE-II forcing. For this study, we use the 62-year period from 1948 to 2009.

228 In data-forced ocean sea ice simulations [e.g., *Danabasoglu et al.*, 2014a], it is nec-
 229 essary to linearly restore sea surface salinity toward climatology in order to maintain a
 230 robust Atlantic Meridional Overturning Circulation (AMOC). For the high and low resolu-
 231 tion simulations we have chosen a piston velocity of 50 m/year (equivalent to a time scale
 232 of one year if we assume a depth scale of 50 m) as our constant of proportionality, which
 233 is consistent with the majority of ocean models described in *Danabasoglu et al.* [2014a].
 234 This restoring term is applied as a salinity source in the top layer of the model, including
 235 under sea ice in proportion to the fraction of open water. The restoring source term is cal-
 236 culated at the beginning of every model day, and the global mean is removed so that it has
 237 no net effect on the total amount of salt.

238 2.4 Resolutions

247 Two model resolutions are used in this study: a low-resolution that requires a mesoscale
 248 eddy closure parameterization (EC60to30) and a high-resolution that is mesoscale eddy-
 249 resolving (RRS18to6). The specifications of the EC60to30 and RRS18to6 meshes are
 250 shown in Table 1. The EC60to30 mesh contains 230 thousand horizontal ocean cells,
 251 which is greater than a standard $1/2^\circ$ uniform grid. Grid cell size varies from 30 to 60 km,
 252 with enhanced resolution in equatorial and polar regions in order to resolve important
 253 equatorial dynamics such as Tropical Instability Waves (Fig. 1). This mesh includes 60
 254 vertical layers ranging from 10 m thick at the surface to 250 m thick in the deep ocean.

255 The high-resolution mesh cell spacing follows the ‘‘Rossby Radius Scaling.’’ The
 256 RRS18to6 mesh was designed to be similar to a $1/10^\circ$ grid, with grid cell size varying
 257 with latitude in proportion to the Rossby radius of deformation. Thus, away from conti-
 258 nental shelves, the mesh resolution is roughly equivalent to the size of mesoscale eddies,
 259 facilitating the model to resolve mesoscale eddy activity within the Antarctic Circumpolar
 260 Current. The resolution for this RRS18to6 mesh ranges from 18 km near the equator to
 261 6 km at the poles, and includes 80 vertical layers ranging from 2 m at the surface to 220 m
 262 at depth.



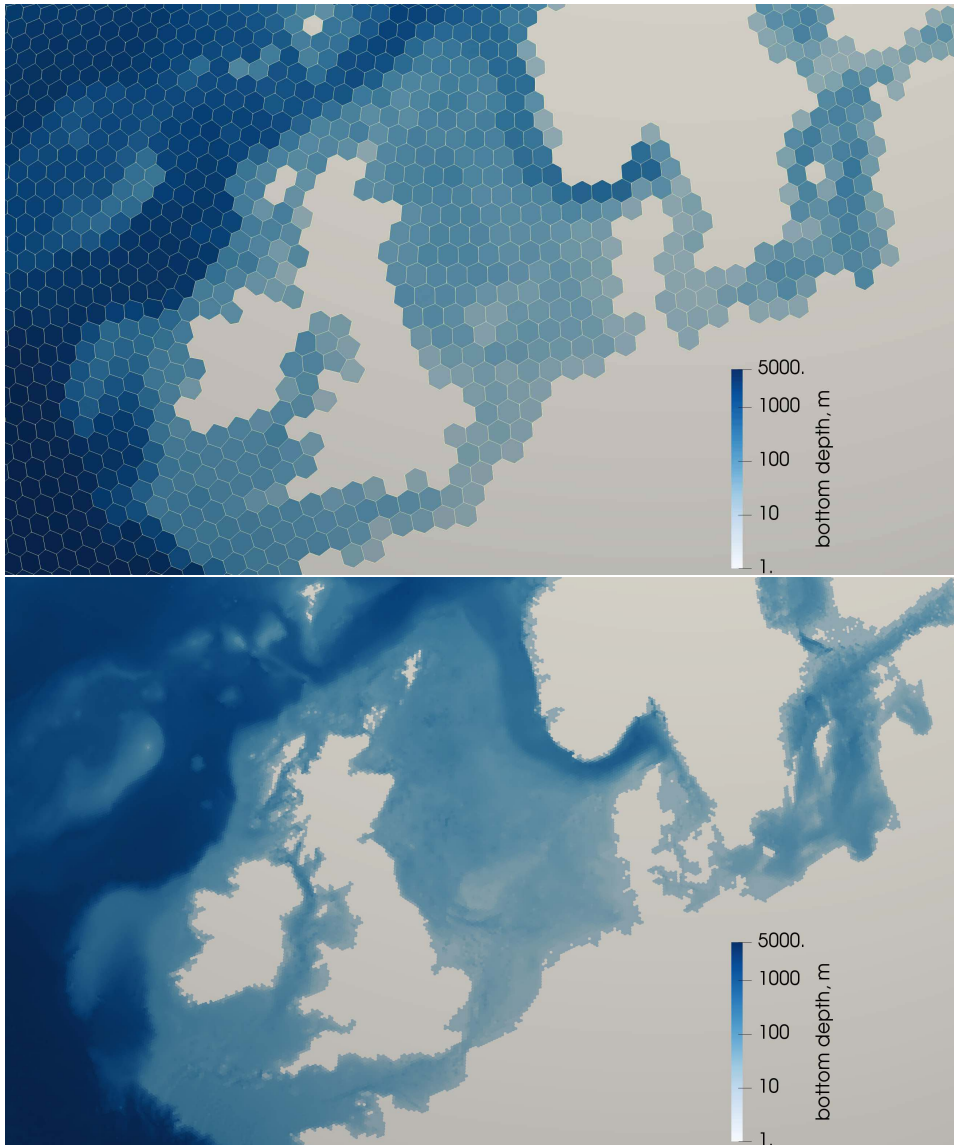
243 **Figure 1.** Grid cell size of the unstructured mesh as a function of latitude for the two standard resolutions.

263 The horizontal meshes were created with an iterative, parallel algorithm for the con-
 264 struction of Spherical Centroidal Voronoi Tessellations [Jacobsen *et al.*, 2013]. Global
 265 meshes are not coastal conforming, i.e. cell edges do not exactly line up along the coast-
 266 line. Rather, a mesh is generated from a grid cell density function on the full sphere.
 267 Then, grid cells with cell centers on the landward side of coastlines² are culled. Sea ice
 268 and ocean components are run on identical meshes so that no horizontal interpolation is
 269 required to compute fluxes between these components. In the ocean, the bottom depth of
 270 each grid cell is generated from a combination of ETOPO1 [Amante and Eakins, 2009]
 271 north of 60°S blended with Bedmap2 [Fretwell *et al.*, 2013] south of 60°S. Each column
 272 uses a partial bottom cell and a minimum thickness of three cells in shallow regions.
 273 Single-cell wide channels are removed from the mesh in polar regions, as the sea ice
 274 model is discretized on an Arakawa B-grid [Arakawa and Lamb, 1977] and requires two
 275 grid cells for sea ice advection. In the low-resolution mesh, the depths of gridcells at the
 276 sills of the Strait of Gibraltar, English Channel, and outlets of the Red Sea, Baltic Sea,
 277 and Persian Gulf are set to the maximum sill depth for that passage to provide adequate
 278 cross-sectional area for transport.

279 2.5 Performance

280 E3SM is designed for high performance computing architectures. Each component
 281 may be scaled up to tens of thousands of processing cores using a combination of mes-
 282 saging (MPI) and threading (OpenMP). E3SM compiles into a single executable,
 283 but each model component may be run either in its own separate partition of MPI ranks,
 284 or stacked within the same partition. The processor layout is adjusted and load-balanced
 285 in order to maximize overall throughput of the coupled system, measured in simulated
 286 years per wall-clock day (SYPD). The simulations presented here were performed on a
 287 project-owned partition of the Blues cluster at Argonne National Laboratory’s Labora-
 288 tory Computing Resource Center. Each node in this partition consists of two 18-core Intel
 289 Xeon “Broadwell” (E5-2697V4, 2.3 GHz) processors and 64 GB dynamic random-access
 290 memory, connected through an Fourteen Data Rate (FDR) InfiniBand network. The low
 291 resolution configuration used 1200 cores for the ocean in one partition, and 320 cores in

² Land regions are taken from a combination of Natural Earth (<http://www.naturalearthdata.com/>) north of 60°S and Bedmap2 [Fretwell *et al.*, 2013] south of 60°S.



244 **Figure 2.** Examples of ocean meshes around the North Sea region for low resolution (EC60to30, top) and
 245 high resolution (RRS18to6, bottom) where hexagons are fine enough that they are indistinguishable from
 246 figure pixels.

292 a second partition that shared sea ice, coupler and data components. Similarly, the high
 293 resolution simulation was partitioned between 3600, 3200, and 3600 cores for ocean, sea
 294 ice, and coupler. The throughput is 10.9 and 0.72 SYPD for low and high resolution,
 295 which translates to 0.34 and 11.17 million CPU hours per century. The coupling interval
 296 is 0.5 hours for each resolution. While the performance is respectable, substantial ongoing
 297 work is directed at improving performance of the MPAS components, including message-
 298 passing optimization, thread optimization, vectorization, and Graphics Processing Unit
 299 acceleration.

2.6 Analysis

Because computational performance is likely to continue to increase faster than I/O and file system performance, we have chosen to perform much of our analysis *in situ* via an analysis member approach. In traditional analysis, data is written to disk and then in a post-processing step is read back into memory for analysis computations. MPAS-Ocean's *in situ* analysis members, in contrast, do not require a post-processing step but are instead computed while MPAS-Ocean is running to produce computationally and data intensive model diagnostics. The analysis member approach has already allowed computation of challenging diagnostics that would be computationally intractable if dependent upon post-processing analysis of data output, e.g., the Okubo-Weiss eddy diagnostics [Woodring *et al.*, 2016], the Eliassen-Palm flux tensor [Saenz *et al.*, 2015; Ringler *et al.*, 2017] as well as Lagrangian particle tracking used for the computation of diffusivity [Wolfram *et al.*, 2015; Wolfram and Ringler, 2017a,b]. This online analysis member approach is also being used within E3SM to compute priority diagnostics to assess simulation quality for fields such as the AMOC and meridional heat transport.

We have also built a Python-based tool, MPAS-Analysis³, for performing post-processed analysis and plotting. With the help of NetCDF Operators (NCO)⁴, MPAS-Analysis can compute climatologies, extract time series and perform interpolation to common reference grids (via remapping operations). The tool supports comparisons between simulation results and a wide variety of observational data sets on either latitude/longitude or polar stereographic grids (the latter being common for many data sets covering polar regions). Alternatively, simulations can be compared against one another to explore the effects of changing parameters, resolution, model physics, meshes and much more. MPAS-Analysis breaks each analysis task into a large number of modular subtasks, allowing each task or subtask to run in parallel, making the production of hundreds of plots relatively efficient. Since MPAS-Analysis can parse the E3SM namelist options and input/output streams of any MPAS model component, tasks are automatically included or excluded, depending on which analysis members and model physics were included in the simulation. The final product of an MPAS-Analysis run is both a user-friendly website with image galleries of all plots and a set of NetCDF files that contain the post-processed data used to create each plot.

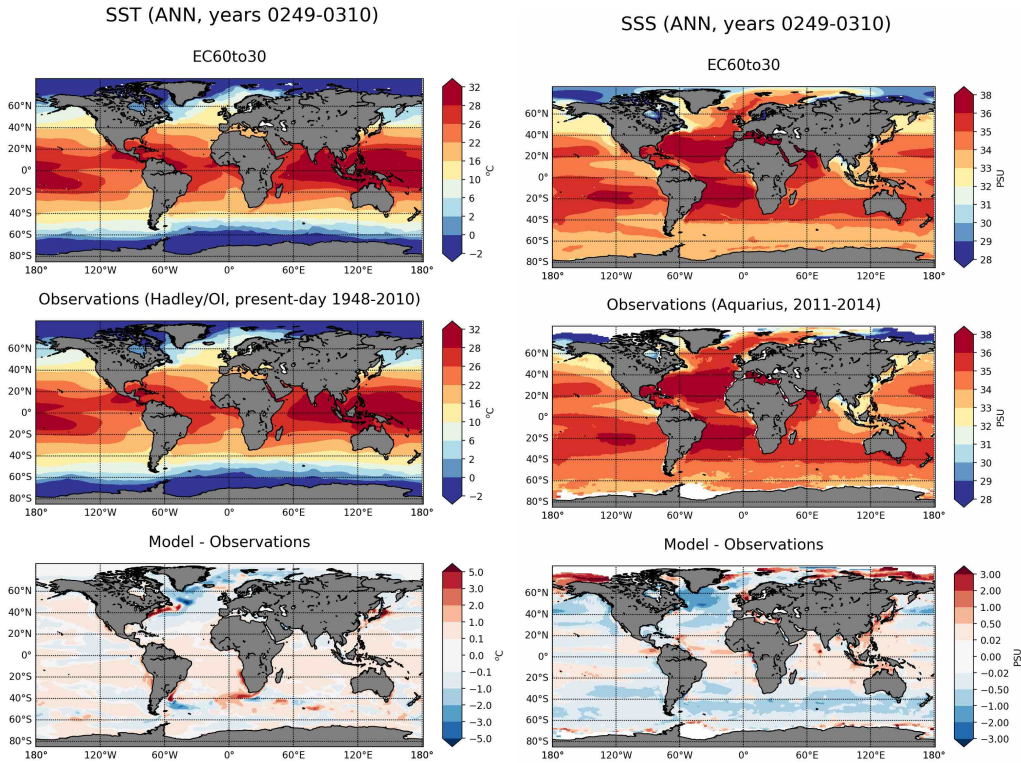
3 Results

3.1 Temperature, salinity, and heat content

A first assessment of the simulated global ocean surface conditions is made by considering the annual average (computed over the last CORE cycle) sea surface temperature (SST) and sea surface salinity (SSS; upper panels in Figure 3), compared with SST observations from the merged Hadley Center-NOAA/OI data set [Hurrell *et al.*, 2008] for the period 1948-2010 and SSS observations from the NASA Aquarius Satellite for the period 2010-2014 (see middle panels of Fig. 3 for the observational fields, while the lower panels show the model-observation biases). Overall the model exhibits a warm SST bias between the midlatitudes and the equator, with mean values smaller than 1°C in most places except for the regions north of the Gulf Stream and Kuroshio Currents, where biases are 5°C or larger. Negative SST biases are found in the Nordic Seas and Labrador Sea, which could be associated with a shift in the position of the modeled Gulf Stream and Kuroshio currents or associated with overly extended sea-ice coverage. The cold bias in the Labrador Sea is also associated with a fresh bias in SSS (lower right panel in Fig. 3). The globally averaged SST, shown in Figure 4, shows a very stable surface temperature with the ex-

³ <https://github.com/MPAS-Dev/MPAS-Analysis>

⁴ <https://github.com/nco/nco>



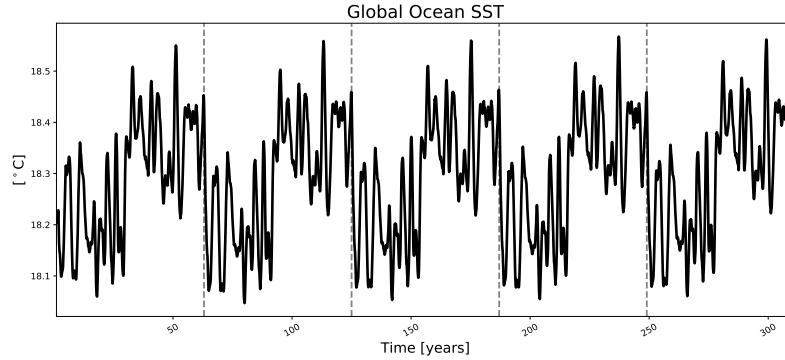
332 **Figure 3.** Sea surface temperature ($^{\circ}\text{C}$, left) and sea surface salinity (psu, right) compared to observations.

348 pected interannual variability (for example, the sudden changes in each mid-CORE cycle
 349 are due to the mid-1970s North Pacific regime shift, *Hare and Mantua* [2000]).

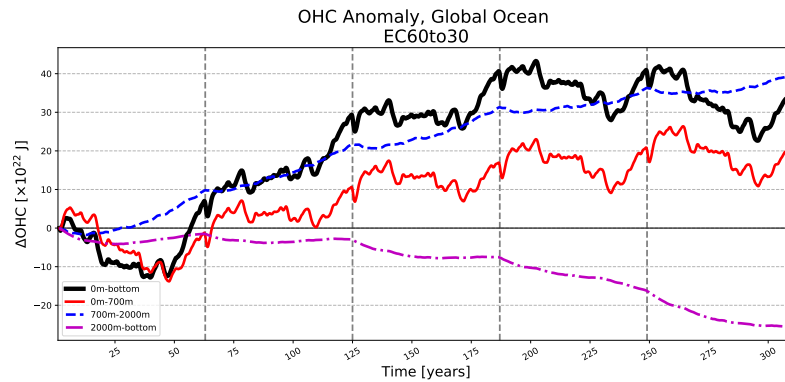
352 The trends of ocean heat content (OHC) integrated over a number of depth ranges
 353 are shown in Figure 5, while OHC and salinity anomalies with depth are presented in Fig-
 354 ure 6. Anomalies are computed with respect to the first year of the simulation in Fig. 5
 355 and with respect to the 4th CORE-cycle last year (year 248) in Fig. 6. The total (surface
 356 to bottom) OHC and upper ocean OHC (0-700m) are stable after the first three CORE
 357 cycles. The OHC integrated over 700-2000m shows a positive trend that is counteracted
 358 by heat loss in the bottom layers. The salinity anomaly trend during the last CORE-cycle
 359 shows the accumulation of a salty anomaly in all of the upper 2000 m, but especially at
 360 the surface and between 300 and 1000 m depth.

365 3.2 Mixed layer depth

366 Fig. 7 shows the mean mixed layer depth (MLD), which is based on the 0.03 kg/m^3
 367 density threshold criterion [*de Boyer Montégut et al.*, 2004] compared to an ARGO cli-
 368 matology [*Holte et al.*, 2017] for Boreal and Austral winter (Fig. 7a and b respectively).
 369 There is a significant shallow bias covering much of the North Atlantic, which is consis-
 370 tent with the modeled surface fresh bias (Fig. 3). The largest of these shallow biases are
 371 in the Labrador and Irminger Seas, which are key locations of North Atlantic Deep Water
 372 (NADW) formation. The shallow bias in the Labrador Sea is broadly consistent with a
 373 number of other CORE forced models (see [*Danabasoglu et al.*, 2014b] their Figure 13).
 374 The CORE forced models with shallower Boreal winter MLD experience weaker AMOC
 375 strengths. This is also seen in MPAS-Ocean (see Figure 10). In contrast, the MLD is too
 376 deep in the northern Western Boundary Currents (WBCs) and their extension regions, as



350 **Figure 4.** Sea surface temperature ($^{\circ}\text{C}$), globally averaged. Vertical lines correspond to CORE-II cycle
351 boundaries.



361 **Figure 5.** Ocean heat content anomaly (10^{22} J), globally averaged, partitioned by depth. Negative trends
362 indicate heat loss from the ocean. Vertical lines correspond to CORE-II cycle boundaries.

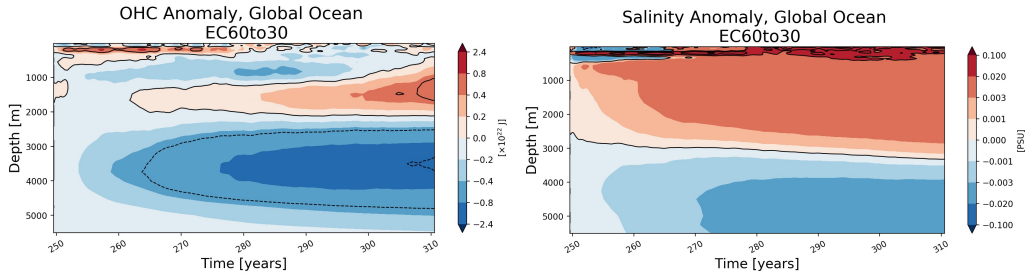
377 well as in the Norwegian Sea. Overall, there is a shallow bias throughout the Southern
378 Hemisphere in Austral summer.

379 In Austral winter, the model exhibits a significant deep MLD bias across most of
380 the Southern Hemisphere. However, the E3SM longitudinal distribution of maximum
381 mixed layer depth between 45S and 65S in the Southern Ocean is very consistent with the
382 ARGO climatology (Fig. 8), suggesting the bias is an offset in the latitudinal position of
383 the deepest MLD in the model compared to the data. However, at high resolution, the lon-
384 gitudinal distribution of modeled (Fig. 8) MLD are deeper than observed. In the Northern
385 Hemisphere, the summer bias is typically slightly shallow and quite small in magnitude.

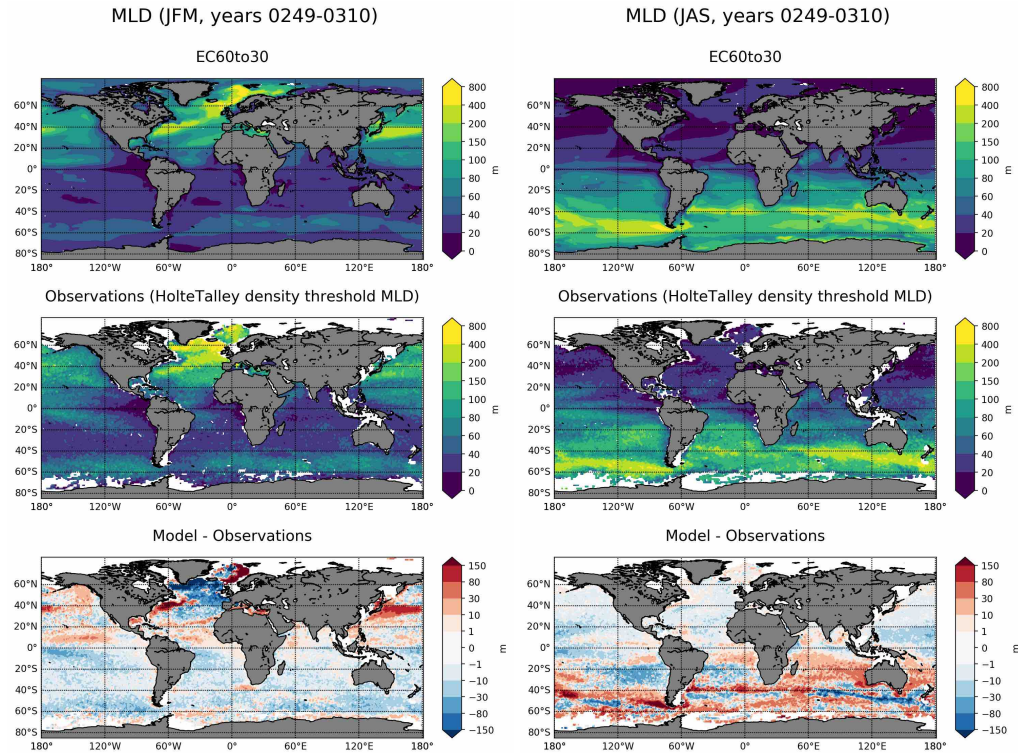
389 3.3 Ocean currents and transport

390 Fig. 9 shows the surface currents for two regions at high resolution (top panels) and
391 a surface drifter climatology [Laurindo et al., 2017] (bottom panels). When mesoscale ed-
392 dies are resolved the strength of the Gulf Stream and separation compare well with obser-
393 vations, consistent with previous studies [e.g., Maltrud and McClean, 2005]. The South-
394 ern Ocean surface currents in the RRS18to6 configuration are close to observations.

395 The strong agreement between drifter observations and model output at high res-
396 olution indicates the capability of MPAS-Ocean to adequately resolve western boundary
397 currents and geostrophic jets such as the Antarctic Circumpolar Current (ACC). The emer-



363 **Figure 6.** Global average anomaly compared with year 248 of ocean heat content (10^{22} J, left) and salinity
 364 (psu, right) as functions of depth, for the fifth CORE cycle.

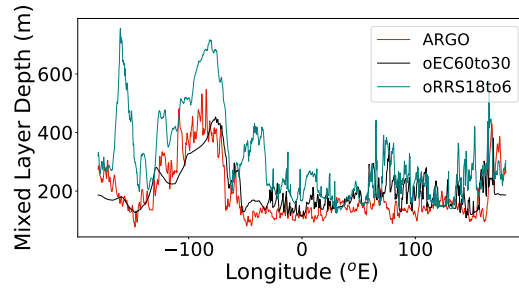


386 **Figure 7.** Mixed layer depth (m) compared to observations.

398 gence of this capability at high resolution is consistent with these current systems being
 399 dependent on mesoscale eddy activity [e.g., *Maltrud and McClean, 2005; Kirtman et al.,*
 400 *2012*]. Thus, it is not surprising that the low resolution E3SM configuration is unable to
 401 accurately simulate the western boundary currents and the ACC (not shown).

419 Figure 10 shows the AMOC averaged over the final CORE cycle for the low resolution
 420 case, and years 25–35 of the high resolution run. The low resolution AMOC (which
 421 is the sum of the Eulerian mean and bolus components) is quite weak, with a maximum
 422 transport of about 10 Sv. When compared with the simulations described in *Danabasoglu*
 423 *et al. [2014a]*, this run is at the low end of overturning strength.

424 Although the AMOC is weak in the low resolution run, it is stable over the final
 425 three CORE cycles, as can be seen in the time series of maximum strength at the RAPID
 426 location (26.5°N , figure 11). The weak overturning is consistent with the generally slug-



387 **Figure 8.** Maximum mixed layer depths (m) between 65°S and 45°S as a function of longitude for both
 388 resolutions, compared to ARGO observations.

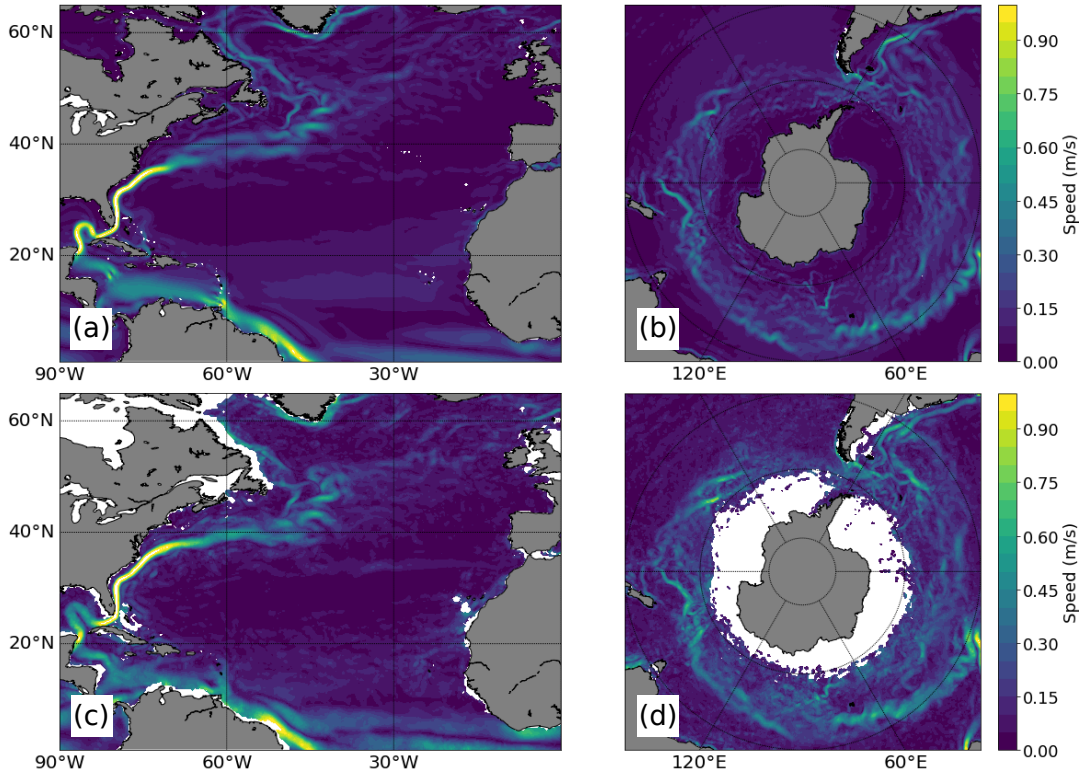
427 gish North Atlantic current transports in the low resolution case (Table 2), but is likely
 428 due to a combination of inter-related effects, such as the GM coefficient, SSS restoring
 429 strength, vertical mixing, and model bathymetry. For example, decreasing the GM coef-
 430 ficient from 1800 to $600\text{m}^2\text{s}^{-1}$ increased the AMOC at 26.5°N by 3 Sv (figure 11). In
 431 another sensitivity test, the piston velocity of SSS restoring was increased by an order of
 432 magnitude (a time scale of about one month), resulting in a strengthening of the AMOC
 433 by 2-3 Sv, but it negatively affected other aspects of the simulation. A spatially variable
 434 GM coefficient may improve circulation in future simulations [*Gent and Danabasoglu,*
 435 2011]. Figure 11 may be directly compared to other ocean models in figure 1 of *Danaba-*
 436 *soglu et al.* [2014a]. E3SM ranges with a GM value of 600 ranges from 9 to 11 Sv over
 437 the last three CORE cycles.

438 Another factor that likely contributes to the weak AMOC is the lack of deep convec-
 439 tion in the Labrador and Irminger Seas (evidenced by a shallow mixed layer depth bias in
 440 Section 3.2). This leaves only the Iceland and Norwegian Seas as sources of NADW for-
 441 mation. The water mass characteristics of the Deep Western Boundary Current (DWBC)
 442 at 26°N are consistent with the relatively warm water formed in the Iceland Basin mixed
 443 with cold overflow from Denmark Strait and the Faroe-Iceland Ridge. However, without
 444 extra model diagnostics it isn't clear what fraction of the DWBC transport is due to annual
 445 formation rates, and how much is recirculation.

446 In contrast to the sluggishness of the low resolution runs, the high resolution case
 447 has a maximum transport (23 Sv) on the high side of the observed value at RAPID and
 448 has a somewhat deeper and enhanced southward return flow, which may be related to the
 449 short duration of the simulation. Since several of the factors that affect low resolution
 450 are not relevant in this case (GM parameterization is turned off, and the Florida Straits
 451 bathymetry is sufficiently resolved), the primary drivers of the AMOC are the SSS restor-
 452 ing and vertical mixing. Unlike at low resolution, there is wintertime deep convection in
 453 the Labrador and Irminger Seas.

454 Table 2 shows the simulated transports through a number of major channels, compar-
 455 ed to observations. Southern Ocean transports at low and high resolution are reason-
 456 able but on the lower side of observations. Like the AMOC, Drake Passage transport is
 457 sensitive to the GM bolus parameter, where the higher value of $1800\text{m}^2\text{s}^{-1}$ resulted in
 458 unreasonably weak transports. Steeper isopycnals in the meridional direction of the South-
 459 ern Ocean were observed in the low-GM case, leading to increased zonal flow via the
 460 thermal wind relation.

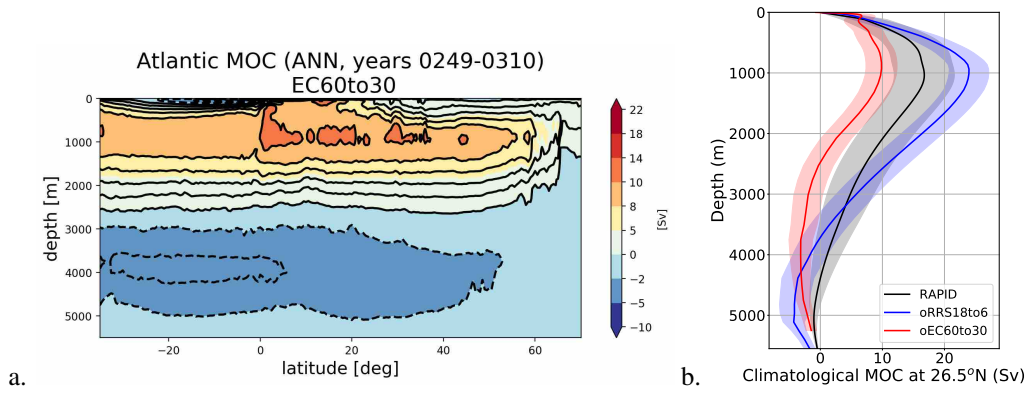
461 As noted in section 2, alteration of the model bathymetry was performed in only five
 462 passages, all of which are associated with marginal seas. As a result of this approach, the
 463 flow through the Straits of Florida between Florida and the Bahamas is quite restricted by
 464 the representation of the islands in the low resolution case, resulting in only 17.6 Sv of



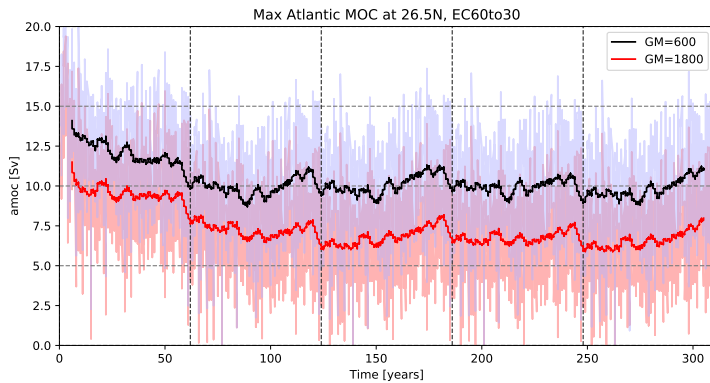
406 **Figure 9.** Mean surface currents (m/s) in Atlantic Ocean (a and c) and Southern Ocean (b and d). The top
 407 row is from the high resolution simulation and the bottom is from the surface drifter climatology of *Laurindo*
 408 *et al.* [2017].

465 transport through this passage. Some minor changes to the bathymetry (such as requiring
 466 at least 2 grid cells spanning the passage) would likely increase the transport here, thus
 467 increasing the strength of the AMOC.

468 The global meridional heat transport (MHT, Figure 12a) reflects the overturning
 469 strength of the simulations. At coarse resolution the values are low compared to esti-
 470 mates, especially in the Southern Hemisphere. At high resolution, heat transport is in-
 471 creased in both hemispheres and is closer to estimates. At low resolution the Atlantic
 472 MHT (Figure 12b) is weak relative to other CORE forced simulation (see [*Danabasoglu*
 473 *et al.*, 2014b] their Figure 6), this is likely related to the weak AMOC and is consistent
 474 with the linear relationship shown in Figure 7 of *Danabasoglu et al.* [2014b].



409 **Figure 10.** Meridional overturning streamfunction (Sv) versus latitude and depth for the EC60to30 with a
 410 GM coefficient of $600\text{m}^2\text{s}^{-1}$ (a) and as a function of depth at 26.5°N for both resolutions (b). These are time
 411 averages of the fifth core cycle for EC60to30, of years 25-35 for the RRS18to6, and of 2004 to 2016 for the
 412 RAPID array.



413 **Figure 11.** Maximum meridional overturning (Sv) at 26.5°N versus time for two values of the GM parameter
 414 (κ) in units of m^2s^{-1} . Light shading shows the monthly average and dark lines are a five-year running
 415 average. Vertical lines are the boundaries of the 62-year CORE cycles.

Table 2. Transport of major current systems: Simulated time-mean transports in Sverdrups through common sections are compared to observational estimates. Simulated transports are of the form mean \pm standard-deviation, while observed transports are of the form best-estimate \pm observational-error. Positive values are north and eastward. These are time averages of the fifth core cycle for EC60to30 and of years 25–35 for the RRS18to6. The EC60to30 run with a GM bolus coefficient of $600\text{m}^2\text{s}^{-1}$ was the primary simulation, and the high GM value of 1800, which has much lower Southern Ocean transports, is shown for comparison. The asterisk indicates estimates from publication.

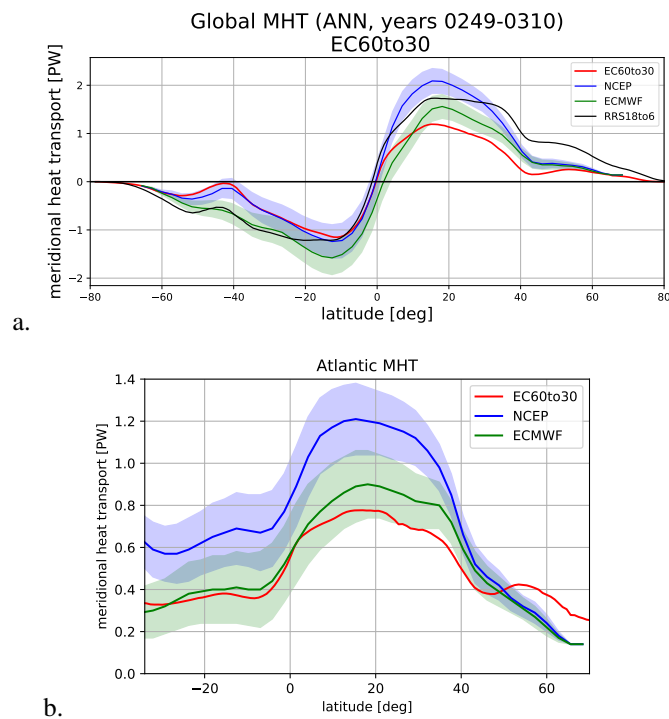
Transect location	EC60to30		RRS18to6	Observations	Observation reference
	GM=1800	GM=600			
Drake Passage	89.8 ± 16.8	127.3 ± 10.6	128.2 ± 8.7	173.0 ± 10.0	[Donohue et al., 2016]
Tasmania-Ant	103.3 ± 19.1	139.4 ± 12.7	147.2 ± 8.3	130.0 ± 20.0	[Whitworth and Peterson, 1985; Nowlin and Klinck, 1986]
Africa-Ant	88.4 ± 16.8	126.0 ± 10.6	129.6 ± 8.5	157.0 ± 10.0	[Ganachaud and Wunsch, 2000; Ganachaud, 2003]
Antilles Inflow	-14.8 ± 2.9	-16.1 ± 3.0	-26.9 ± 4.7	150.0 ± 30.0	[Ganachaud and Wunsch, 2000; Ganachaud, 2003]*
Mona Passage	-1.7 ± 1.0	-1.4 ± 1.3	-1.0 ± 1.2	-18.4 ± 4.7	[Johns et al., 2002; Roemmich, 1981]
Windward Passage	1.0 ± 2.0	-0.2 ± 2.3	3.3 ± 4.8	-2.6 ± 1.2	[Johns et al., 2002; Roemmich, 1981]
Florida-Cuba	15.4 ± 1.4	15.4 ± 1.4	24.5 ± 3.5	6.0 ± 3.0	[Johns et al., 2002; Roemmich, 1981]
Florida-Bahamas	15.1 ± 1.1	17.6 ± 1.6	30.1 ± 2.7	31.0 ± 1.5	[Johns et al., 2002; Roemmich, 1981]
Indonesian Throughflow	-11.0 ± 3.6	-10.2 ± 3.7	-13.4 ± 2.8	31.5 ± 1.5	[Johns et al., 2002; Roemmich, 1981]
Agulhas	-68.7 ± 5.6	-72.2 ± 5.4	-57.7 ± 22.4	-15.0 ± 4.0	[Sprintall et al., 2009]
Mozambique Channel	-18.7 ± 6.7	-15.8 ± 6.4	-22.0 ± 6.0	-70.0 ± 20.0	[Bryden and Beal, 2001]
Bering Strait	0.9 ± 0.5	1.1 ± 0.5	1.5 ± 0.5	-16.0 ± 13.0	[van der Werf et al., 2010]
Lancaster Sound	0.2 ± 0.3	0.3 ± 0.4	1.6 ± 0.4	0.8 ± 0.3	[Roach et al., 1995]
Fram Strait	-2.5 ± 1.1	-3.5 ± 1.2	-1.3 ± 1.3	0.8 ± 0.3	[Prinsenberg and Hamilton, 2005]
Robeson Channel	0.0 ± 0.0	0.0 ± 0.0	-1.1 ± 0.4	-3.0 ± 3.0	[Schauer et al., 2004]
				-0.7 ± 0.2	[Maltrud and McClean, 2005]

402

403

404

405



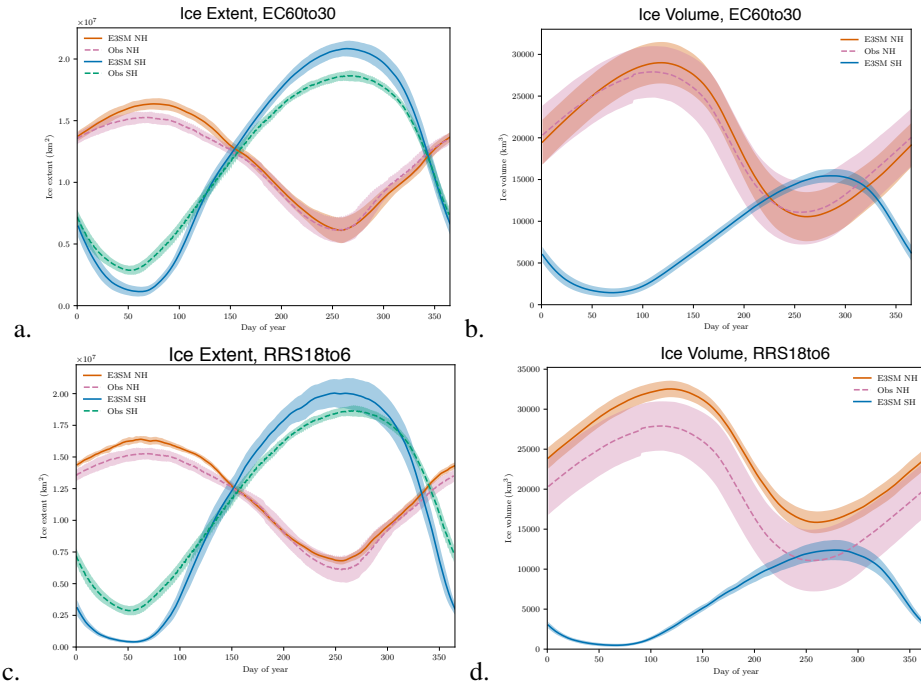
416 **Figure 12.** Meridional heat transport (PW) as a function of latitude for two resolutions, compared to mean
 417 reanalysis climatology from NCEP and ECMWF [*Trenberth and Caron, 2001*], for the globe (a) and the
 418 Atlantic (b). Shading indicates one standard deviation from the mean.

3.4 Sea ice

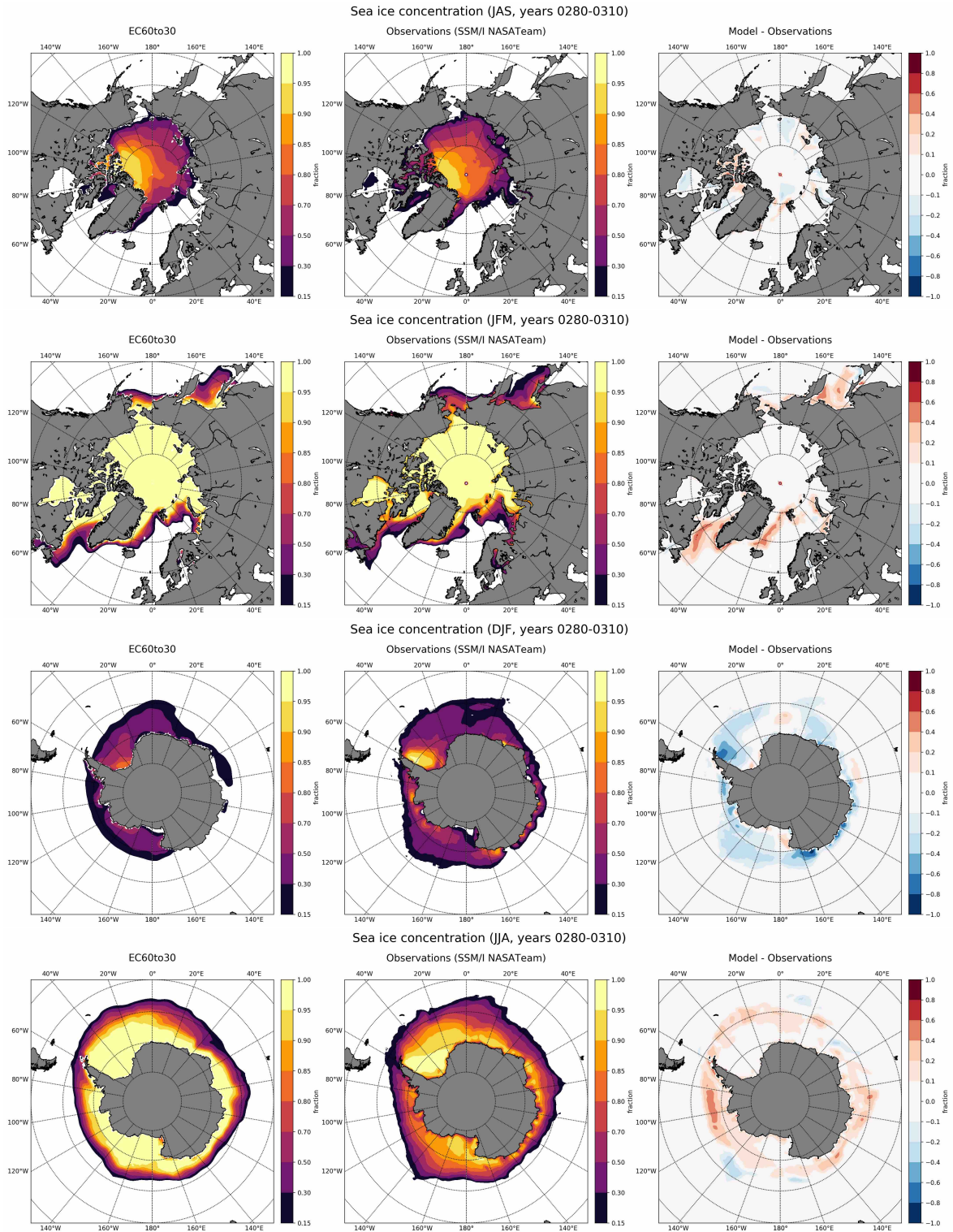
Sea ice has a significant effect on the ocean state. Rejection of salt during sea-ice formation helps drive the thermohaline circulation [Killworth, 1983], while northward transport of fresh sea ice in the Southern Ocean affects water mass transformation [Abernathey et al., 2016]. Consequently, it is important to accurately reproduce the sea-ice state for ocean simulations. Here we examine the sea-ice results for E3SM on the EC60to30 mesh.

Total sea-ice extent (area with sea-ice concentration greater than 15%) is shown in Figure 13 for E3SM output and compared against SSM/I observations for the northern [Cavalieri and Parkinson, 2012; Parkinson et al., 1999] and southern hemisphere [Parkinson and Cavalieri, 2012; Zwally et al., 2002]. The mean and standard deviation for observational years 1979 to 2009 are shown, and compared against the equivalent model years (280 to 310) for the fifth CORE cycle of model output for the EC60to30 resolution, and for years 1–37 of the RRS18to6 simulation. In the northern hemisphere there is generally good agreement between the model and observation, especially in winter, although E3SM over-estimates sea-ice extent in the northern hemisphere in summer. In the southern hemisphere, the model has too large a seasonal cycle compared to observations, although, again, agreement is generally good. Figure 13b compares total northern hemisphere sea-ice volume between model output and the Pan-Arctic Ice Ocean Modeling and Assimilation System (PIOMAS) assimilated data product [Schweiger et al., 2011a]. Inter-annual variance of ice volume is larger than ice area, but model and the PIOMAS product agree well, with the model capturing the seasonal cycle of sea-ice volume. Due to a lack of reliable data product for the southern hemisphere, we only show model results for this region. Higher ice volume in the high-resolution simulation (Figure 13d) is expected due to the earlier CORE-II forcing years.

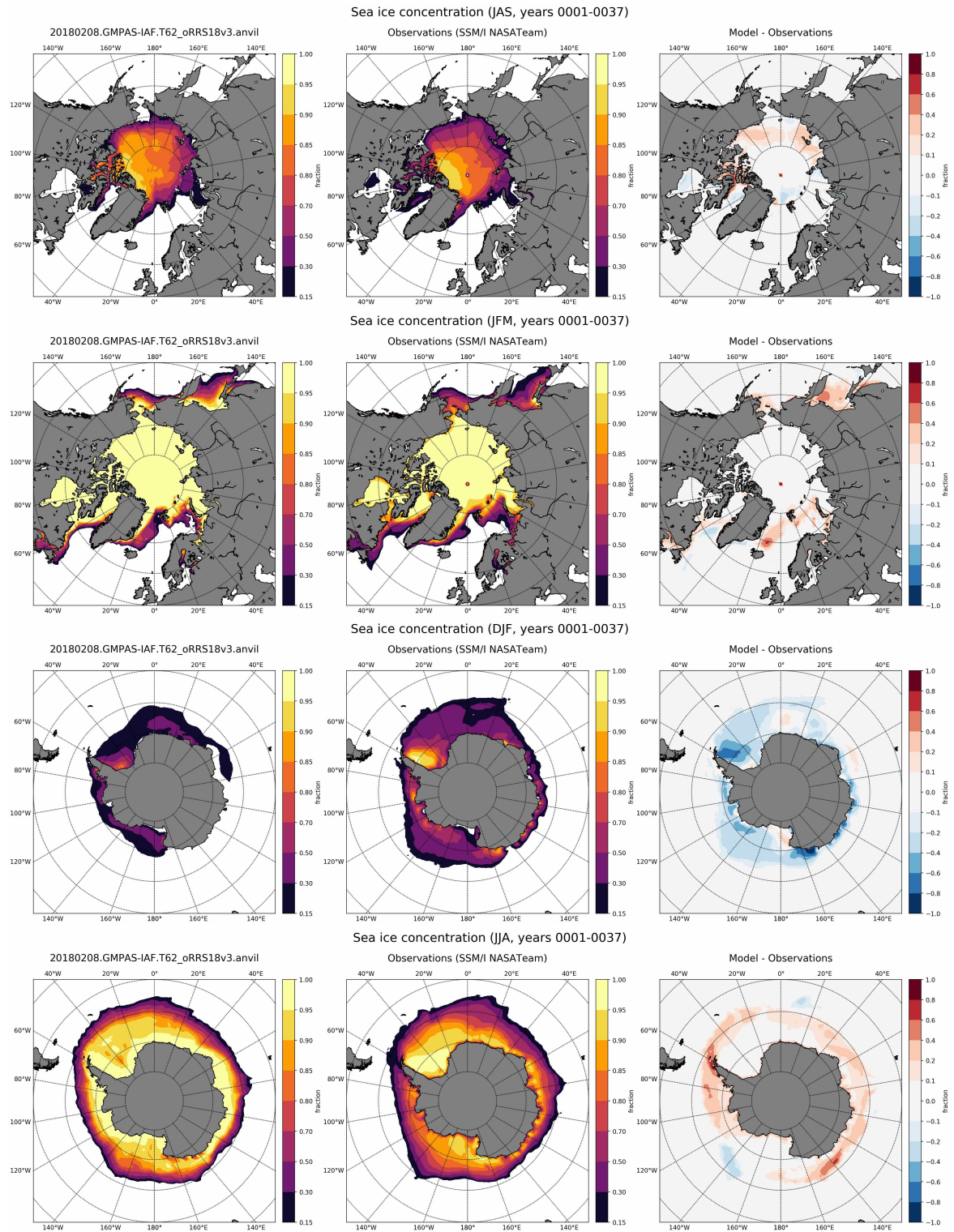
In Figures 14 and 15 we show spatial climatological maps of sea ice concentration for E3SM and for SSM/I satellite observations, produced with the NASATeam algorithm [Cavalieri et al., 1996, updated yearly]. Climatological maps are generated for the years 1979 to 2009 and for winter (January, February, and March in the northern hemisphere, and June, July, and August in the southern hemisphere) and summer (July, August, and September in the northern hemisphere, and December, January, and February in the southern hemisphere) seasons. In general E3SM does a good job of reproducing the observational climatology of ice concentration and the ice-pack edge. Good agreement is obtained in the Arctic during both seasons, especially during summer, with E3SM displaying too much ice in the Labrador and Greenland seas in winter. In the southern hemisphere, E3SM shows too much ice concentration in winter, whereas in summer the model displays too little ice in the Weddell Sea and virtually no sea ice along the East Antarctic coast (60-160°E).



513 **Figure 13.** Total ice extent climatology (area with ice concentration > 15%, km²) (a,c) and total ice volume
 514 climatology (b,d) for the northern and southern hemispheres, for E3SM results and observations, each for
 515 low resolution (a,b) and high resolution (c,d). Ice extent uses SSM/I observations [Cavalieri and Parkinson,
 516 2012; Parkinson and Cavalieri, 2012] and northern hemisphere volume observations come from PIOMAS
 517 [Schweiger et al., 2011b]. The color bands represent ±1 standard deviation of the climatology. No southern
 518 hemisphere observational results are shown for ice volume.



519 **Figure 14.** Sea ice concentration (normalized fraction) versus observations (SSM/I NASATeam algorithm
 520 [Cavalieri *et al.*, 1996, updated yearly]), where both are compared over the period 1979–2009, for the low
 521 resolution simulation (EC60to30).



522 **Figure 15.** Same as Figure 14 but for high resolution (RRS18to6), averaged over the duration of the simu-
 523 tion.

524

3.5 High resolution diagnostics

525

526

527

528

529

530

531

532

533

The sea surface height variability averaged over 10 years of the E3SM run is shown in Fig. 16 against the AVISO satellite product [Ablain *et al.*, 2015]. E3SM reproduces much of the observed SSH variability seen in observations. There are slight biases near the Agulhas, where eddy shedding is too regular, a common bias in eddy resolving ocean models [e.g., Maltrud and McClean, 2005]. There is also too little variability in the Northwest Corner of the North Atlantic current. Finally, we note that the background SSH variability in E3SM is higher than AVISO. This is most likely due to the split explicit time-stepping in MPAS-Ocean, which does not filter gravity waves, whereas these waves are filtered by AVISO and implicit models of the barotropic component.

534

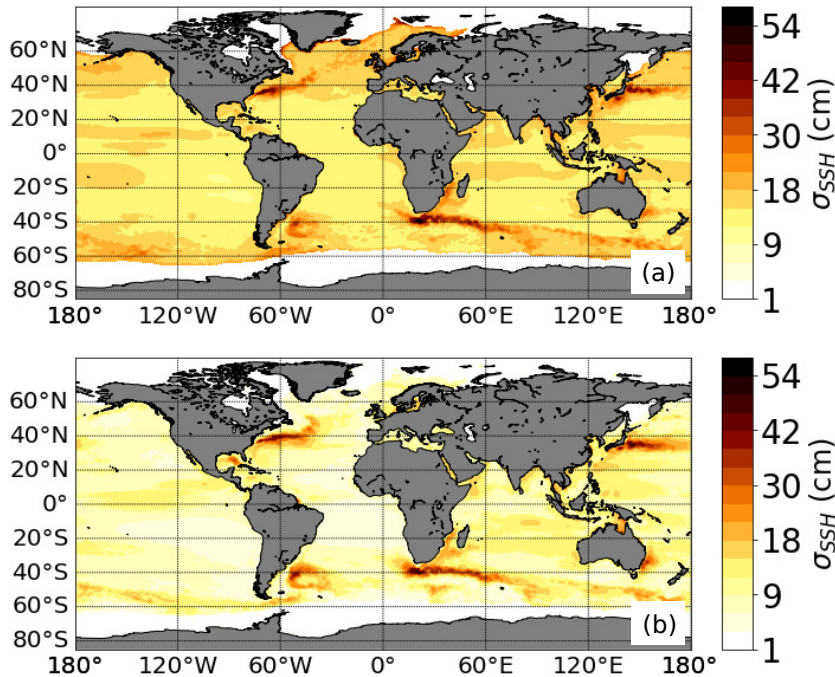
535

536

537

538

Fig. 17 shows the eddy kinetic energy (EKE) averaged over years 25–35. E3SM EKE is higher than other eddy resolving ocean configurations. This is likely due to the improved, 80-layer, vertical grid used in E3SM, consistent with the results of Stewart *et al.* [2017]. The distribution of EKE in the Northwest Corner of the high-resolution simulation compares well with observations.



539

Figure 16. SSH variability (cm) from (a) E3SM v1 high resolution (averaged over years 25 and 35 inclusive) and (b) AVISO

540

543

4 Conclusions

544

545

546

547

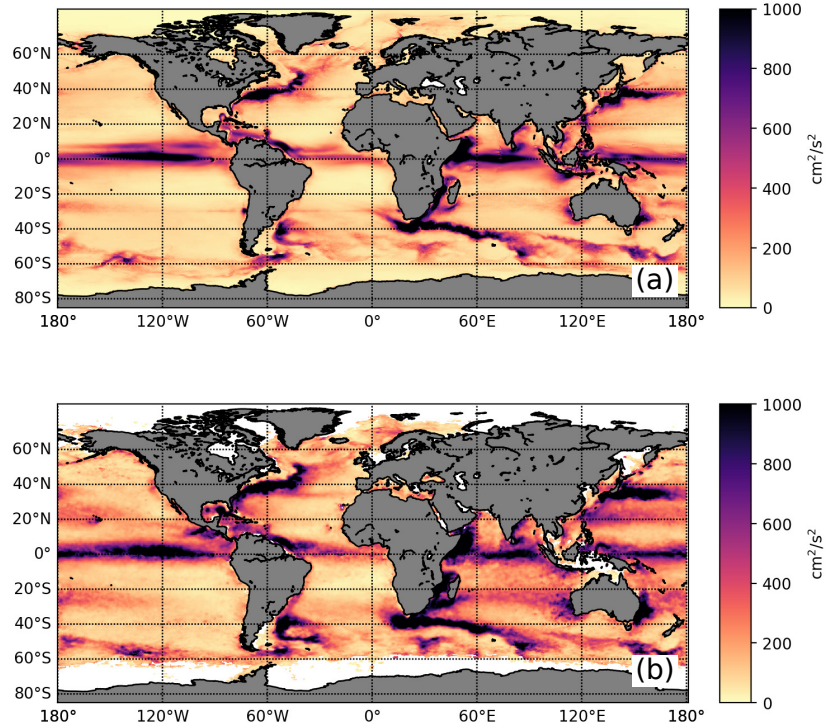
548

549

550

551

This paper is one of many to present model configurations and simulation results for E3SM. Here we focus on coupled ocean and sea ice components, while others present results from stand-alone sea ice, land ice, and fully coupled simulations. Model results demonstrate the ability of E3SM to produce realistic currents, meridional heat transport, sea ice coverage, and distributions of sea surface temperature and salinity in this configuration where the atmosphere is CORE-II forcing. The high-resolution simulation shows the successful use of E3SM for strongly eddying flows, e.g., for western boundary currents as well as the ACC. The solution fidelity for mesoscale dynamics in a multi-resolution



541 **Figure 17.** Eddy kinetic energy (cm^2/s^2) from (a) E3SM v1 high resolution simulation (averaged over years
 542 25-35) (b) Surface drifter climatology [Laurindo et al., 2017].

552 context will enable E3SM to resolve the mesoscale oceanic turbulence contributions to the
 553 global climate system in select regions of the global ocean instead of uniform high resolu-
 554 tion.

555 Future applications employing enhanced regional refinement will provide novel di-
 556 rections of scientific inquiry. Many research topics will greatly benefit from the unique
 557 multi-physics and multi-resolution capabilities of E3SM, including: coupled ocean-land-
 558 ice interactions; coastal studies of local sea level rise impacts; ocean-atmospheric feed-
 559 backs such as Eastern boundary current regions; and high-latitude dynamics which are de-
 560 pendent upon a smaller Rossby radius of deformation. In the long term, variable-resolution
 561 meshes provide a lower computational cost, integrated approach to understanding local-
 562 ized climate impacts within the larger earth system. New algorithmic approaches will be
 563 needed to fully realize these efforts, particularly advanced time stepping approaches for
 564 variable resolution meshes such that the model timestep is not dictated by the smallest cell
 565 size, improved, scale-aware, sub-grid scale parameterizations, and performance optimiza-
 566 tion for unstructured meshes on new architectures. Current research by the authors and
 567 their collaborators is already making inroads in these areas, with the goal of near-term,
 568 measurable improvements in E3SM.

569 Most IPCC-class coupled climate models have had decades of development to reach
 570 their current level of fidelity and efficiency. As a brand new model, E3SM will have am-
 571 ple opportunity for improvement in the coming years, but has already shown proficiency
 572 in computational performance and in reproducing twentieth-century climate. These initial
 573 simulations with standard configurations are just the first step. E3SM's multi-resolution
 574 approach to global and regional climate modeling paves the way to a better understanding
 575 of the changing earth system at both the large and small scales.

Acknowledgments

This research was supported as part of the Energy Exascale Earth System Model (E3SM) project, funded by the U.S. Department of Energy, Office of Science, Office of Biological and Environmental Research. E3SM simulations are conducted at: Argonne Leadership Computing Facility (contract DE-AC02-06CH11357); National Energy Research Scientific Computing Center (DE-AC05-00OR22725); Oak Ridge Leadership Computing Facility (DE-AC05-00OR22725); Argonne Nat. Lab. high-performance computing cluster, provided by BER Earth System Modeling; and Los Alamos Nat. Lab. Institutional Computing, US DOE NNSA (DE-AC52-06NA25396).

References

- Abernathy, R., I. Cerovecki, P. R. Holland, E. Newsom, M. Mazloff, and L. D. Talley (2016), Southern Ocean Water Mass Transformation Driven by Sea Ice, *Nature Geoscience*, *9*, 596–601, doi:10.1038/ngeo2749.
- Ablain, M., A. Cazenave, G. Larnicol, M. Balmaseda, P. Cipollini, Y. Faugère, M. J. Fernandes, O. Henry, J. A. Johannessen, P. Knudsen, O. Andersen, J. Legeais, B. Meyssignac, N. Picot, M. Roca, S. Rudenko, M. G. Scharffenberg, D. Stammer, G. Timms, and J. Benveniste (2015), Improved sea level record over the satellite altimetry era (1993–2010) from the Climate Change Initiative project, *Ocean Sci.*, *11*(1), 67–82, doi:10.5194/os-11-67-2015.
- Adcroft, A., and J.-M. Campin (2004), Rescaled height coordinates for accurate representation of free-surface flows in ocean circulation models, *Ocean Modelling*, *7*, 269–284, doi:10.1016/j.ocemod.2003.09.003.
- Amante, C., and B. Eakins (2009), ETOPO1 1 arc-minute global relief model: Procedures, data sources and analysis, *NOAA Technical Memorandum NESDIS NGDC-24. National Geophysical Data Center, NOAA.*, doi:10.7289/V5C8276M.
- Arakawa, A., and V. R. Lamb (1977), Computational Design of the Basic Dynamical Processes of the UCLA General Circulation Model, in *Methods in Computational Physics: Advances in Research and Applications, General Circulation Models of the Atmosphere*, vol. 17, edited by J. Chang, pp. 173–265, Elsevier, doi:10.1016/B978-0-12-460817-7.50009-4.
- Asay-Davis, X. S., N. C. Jourdain, and Y. Nakayama (2017), Developments in Simulating and Parameterizing Interactions Between the Southern Ocean and the Antarctic Ice Sheet, *Current Climate Change Reports*, *3*(4), 316–329, doi:10.1007/s40641-017-0071-0.
- Bitz, C. M., and W. H. Lipscomb (1999), An energy-conserving thermodynamic model of sea ice, *Journal of Geophysical Research: Oceans*, *104*(C7), 15,669–15,677, doi:10.1029/1999JC900100.
- Briegleb, B. P., and B. Light (2007), A Delta-Eddington multiple scattering parameterization for solar radiation in the sea ice component of the Community Climate System Model, *Tech. Rep. NCAR/TN-472+STR*, National Center for Atmospheric Research, Boulder, Colorado USA.
- Bryden, H. L., and L. M. Beal (2001), Role of the Agulhas Current in Indian Ocean circulation and associated heat and freshwater fluxes, *Deep Sea Research Part I: Oceanographic Research Papers*, *48*(8), 1821–1845, doi:10.1016/S0967-0637(00)00111-4.
- Cavalieri, D. J., and C. L. Parkinson (2012), Arctic sea ice variability and trends, 1979–2010, *The Cryosphere*, *6*(4), 881–889, doi:10.5194/tc-6-881-2012.
- Cavalieri, D. J., C. L. Parkinson, P. Gloersen, and H. J. Zwally (1996, updated yearly), Sea Ice Concentrations from Nimbus-7 SMMR and DMSP SSM/I-SSMIS Passive Microwave Data, Version 1, *Tech. rep.*, NASA National Snow and Ice Data Center Distributed Active Archive Center, Boulder, Colorado USA, doi:10.5067/8GQ8LZQVL0VL.
- Chen, Q., T. Ringler, and P. R. Gent (2016), Extending a potential vorticity transport eddy closure to include a spatially-varying coefficient, *Computers & Mathematics with Appli-*

- 628 *cations*, 71(11), 2206 – 2217, doi:<https://doi.org/10.1016/j.camwa.2015.12.041>, proceed-
 629 ings of the conference on Advances in Scientific Computing and Applied Mathematics.
 630 A special issue in honor of Max Gunzburger’s 70th birthday.
- 631 Craig, A. P., M. Vertenstein, and R. Jacob (2012), A new flexible coupler for earth system
 632 modeling developed for CCSM4 and CESM1, *The International Journal of High Perform-*
 633 *ance Computing Applications*, 26(1), 31–42, doi:[10.1177/1094342011428141](https://doi.org/10.1177/1094342011428141).
- 634 Danabasoglu, G., S. G. Yeager, D. Bailey, E. Behrens, M. Bentsen, D. Bi, A. Bias-
 635 toch, C. Böning, A. Bozec, V. M. Canuto, C. Cassou, E. Chassignet, A. C. Coward,
 636 S. Danilov, N. Diansky, H. Drange, R. Farneti, E. Fernandez, P. G. Fogli, G. For-
 637 get, Y. Fujii, S. M. Griffies, A. Gusev, P. Heimbach, A. Howard, T. Jung, M. Kel-
 638 ley, W. G. Large, A. Leboissetier, J. Lu, G. Madec, S. J. Marsland, S. Masina,
 639 A. Navarra, A. George Nurser, A. Pirani, D. Salas y Méliá, B. L. Samuels, M. Schein-
 640 ert, D. Sidorenko, A.-M. Treguier, H. Tsujino, P. Uotila, S. Valcke, A. Voltaire, and
 641 Q. Wang (2014a), North Atlantic simulations in Coordinated Ocean-ice Reference Ex-
 642 periments phase II (CORE-II). Part I: Mean states, *Ocean Modelling*, 73, 76–107, doi:
 643 [10.1016/j.ocemod.2013.10.005](https://doi.org/10.1016/j.ocemod.2013.10.005).
- 644 Danabasoglu, G., S. G. Yeager, D. Bailey, E. Behrens, M. Bentsen, D. Bi, A. Bias-
 645 toch, C. Böning, A. Bozec, V. M. Canuto, C. Cassou, E. Chassignet, A. C. Coward,
 646 S. Danilov, N. Diansky, H. Drange, R. Farneti, E. Fernandez, P. G. Fogli, G. Forget,
 647 Y. Fujii, S. M. Griffies, A. Gusev, P. Heimbach, A. Howard, T. Jung, M. Kelley, W. G.
 648 Large, A. Leboissetier, J. Lu, G. Madec, S. J. Marsland, S. Masina, A. Navarra, A. J.
 649 George Nurser, A. Pirani, D. S. y Méliá, B. L. Samuels, M. Scheinert, D. Sidorenko,
 650 A.-M. Treguier, H. Tsujino, P. Uotila, S. Valcke, A. Voltaire, and Q. Wang (2014b),
 651 North Atlantic simulations in Coordinated Ocean-ice Reference Experiments phase II
 652 (CORE-II). Part I: Mean states, *Ocean Modelling*, 73, 76–107, doi:[10.1016/j.ocemod.](https://doi.org/10.1016/j.ocemod.2013.10.005)
 653 [2013.10.005](https://doi.org/10.1016/j.ocemod.2013.10.005).
- 654 Danabasoglu, G., S. G. Yeager, W. M. Kim, E. Behrens, M. Bentsen, D. Bi, A. Biastoch,
 655 R. Bleck, C. Böning, A. Bozec, V. M. Canuto, C. Cassou, E. Chassignet, A. C. Coward,
 656 S. Danilov, N. Diansky, H. Drange, R. Farneti, E. Fernandez, P. G. Fogli, G. Forget,
 657 Y. Fujii, S. M. Griffies, A. Gusev, P. Heimbach, A. Howard, M. Ilicak, T. Jung, A. R.
 658 Karspeck, M. Kelley, W. G. Large, A. Leboissetier, J. Lu, G. Madec, S. J. Marsland,
 659 S. Masina, A. Navarra, A. G. Nurser, A. Pirani, A. Romanou, D. Salas y Méliá, B. L.
 660 Samuels, M. Scheinert, D. Sidorenko, S. Sun, A.-M. Treguier, H. Tsujino, P. Uotila,
 661 S. Valcke, A. Voltaire, Q. Wang, and I. Yashayaev (2016), North Atlantic simulations
 662 in Coordinated Ocean-ice Reference Experiments phase II (CORE-II). Part II: Inter-
 663 annual to decadal variability, *Ocean Modelling*, 97, 65–90, doi:[10.1016/j.ocemod.2015.](https://doi.org/10.1016/j.ocemod.2015.11.007)
 664 [11.007](https://doi.org/10.1016/j.ocemod.2015.11.007).
- 665 Dasgupta, G. (2003), Interpolants within Convex Polygons: Wachspress’ Shape Functions,
 666 *J. Aerospac. Eng.*, 16, 1–8, doi:[10.1061/\(ASCE\)0893-1321\(2003\)16:1\(1\)](https://doi.org/10.1061/(ASCE)0893-1321(2003)16:1(1)).
- 667 de Boyer Montégut, C., G. Madec, A. S. Fischer, A. Lazar, and D. Iudicone (2004),
 668 Mixed layer depth over the global ocean: An examination of profile data and a profile-
 669 based climatology, *Journal of Geophysical Research: Oceans*, 109(C12), doi:[10.1029/](https://doi.org/10.1029/2004JC002378)
 670 [2004JC002378](https://doi.org/10.1029/2004JC002378).
- 671 Donohue, K. A., K. L. Tracey, D. R. Watts, M. P. Chidichimo, and T. K. Chereskin
 672 (2016), Mean Antarctic Circumpolar Current transport measured in Drake Passage,
 673 *Geophysical Research Letters*, 43(22), 2016GL070,319, doi:[10.1002/2016GL070319](https://doi.org/10.1002/2016GL070319).
- 674 Downes, S. M., R. Farneti, P. Uotila, S. M. Griffies, S. J. Marsland, D. Bailey, E. Behrens,
 675 M. Bentsen, D. Bi, A. Biastoch, C. Böning, A. Bozec, V. M. Canuto, E. Chassignet,
 676 G. Danabasoglu, S. Danilov, N. Diansky, H. Drange, P. G. Fogli, A. Gusev, A. Howard,
 677 M. Ilicak, T. Jung, M. Kelley, W. G. Large, A. Leboissetier, M. Long, J. Lu, S. Masina,
 678 A. Mishra, A. Navarra, A. George Nurser, L. Patara, B. L. Samuels, D. Sidorenko,
 679 P. Spence, H. Tsujino, Q. Wang, and S. G. Yeager (2015), An assessment of Southern
 680 Ocean water masses and sea ice during 1988–2007 in a suite of interannual CORE-II
 681 simulations, *Ocean Modelling*, 94, 67–94, doi:[10.1016/j.ocemod.2015.07.022](https://doi.org/10.1016/j.ocemod.2015.07.022).

- 682 Dukowicz, J. K., and J. R. Baumgardner (2000), Incremental Remapping as a Trans-
 683 port/Advection Algorithm, *Journal of Computational Physics*, *160*(1), 318–335, doi:
 684 10.1006/jcph.2000.6465.
- 685 Evans, K., P. Lauritzen, S. Mishra, R. Neale, M. Taylor, and J. Tribbia (2013), AMIP sim-
 686 ulation with the CAM4 spectral element dynamical core, *J. Climate*, *26*(3), 689–709.
- 687 Fretwell, P., H. D. Pritchard, D. G. Vaughan, J. L. Bamber, N. E. Barrand, R. Bell,
 688 C. Bianchi, R. G. Bingham, D. D. Blankenship, G. Casassa, G. Catania, D. Cal-
 689 lens, H. Conway, A. J. Cook, H. F. J. Corr, D. Damaske, V. Damm, F. Ferracci-
 690 oli, R. Forsberg, S. Fujita, Y. Gim, P. Gogineni, J. A. Griggs, R. C. A. Hindmarsh,
 691 P. Holmlund, J. W. Holt, R. W. Jacobel, A. Jenkins, W. Jokat, T. Jordan, E. C. King,
 692 J. Kohler, W. Krabill, M. Riger-Kusk, K. A. Langley, G. Leitchenkov, C. Leuschen,
 693 B. P. Luyendyk, K. Matsuoka, J. Mouginot, F. O. Nitsche, Y. Nogi, O. A. Nost, S. V.
 694 Popov, E. Rignot, D. M. Rippin, A. Rivera, J. Roberts, N. Ross, M. J. Siegert, A. M.
 695 Smith, D. Steinhage, M. Studinger, B. Sun, B. K. Tinto, B. C. Welch, D. Wilson,
 696 D. A. Young, C. Xiangbin, and A. Zirizzotti (2013), Bedmap2: improved ice bed,
 697 surface and thickness datasets for Antarctica, *The Cryosphere*, *7*(1), 375–393, doi:
 698 10.5194/tc-7-375-2013.
- 699 Ganachaud, A. (2003), Large-scale mass transports, water mass formation, and diffusivi-
 700 ties estimated from World Ocean Circulation Experiment (WOCE) hydrographic data,
 701 *Journal of Geophysical Research: Oceans*, *108*(C7), 3213, doi:10.1029/2002JC001565.
- 702 Ganachaud, A., and C. Wunsch (2000), Improved estimates of global ocean circulation,
 703 heat transport and mixing from hydrographic data, *Nature*, *408*(6811), 453–457, doi:
 704 10.1038/35044048.
- 705 Gent, P. R., and G. Danabasoglu (2011), Response to increasing southern hemisphere
 706 winds in cesm4, *Journal of Climate*, *24*(19), 4992–4998, doi:10.1175/JCLI-D-10-05011.
 707 1.
- 708 Gent, P. R., and J. C. McWilliams (1990), Isopycnal Mixing in Ocean Circulation Mod-
 709 els, *Journal of Physical Oceanography*, *20*(1), 150–155, doi:10.1175/1520-0485(1990)
 710 020<0150:IMIOCM>2.0.CO;2.
- 711 Griffies, S. M., A. Biastoch, C. Böning, F. Bryan, G. Danabasoglu, E. P. Chassignet,
 712 M. H. England, R. Gerdes, H. Haak, R. W. Hallberg, W. Hazeleger, J. Jungclaus, W. G.
 713 Large, G. Madec, A. Pirani, B. L. Samuels, M. Scheinert, A. S. Gupta, C. A. Severi-
 714 jns, H. L. Simmons, A. M. Treguier, M. Winton, S. Yeager, and J. Yin (2009), Coor-
 715 dinated Ocean-ice Reference Experiments (COREs), *Ocean Modelling*, *26*(1-2), 1–46,
 716 doi:10.1016/j.ocemod.2008.08.007.
- 717 Griffies, S. M., J. Yin, P. J. Durack, P. Goddard, S. C. Bates, E. Behrens, M. Bentsen,
 718 D. Bi, A. Biastoch, C. W. Böning, A. Bozec, E. Chassignet, G. Danabasoglu,
 719 S. Danilov, C. M. Domingues, H. Drange, R. Farneti, E. Fernandez, R. J. Greatbatch,
 720 D. M. Holland, M. Ilicak, W. G. Large, K. Lorbacher, J. Lu, S. J. Marsland, A. Mishra,
 721 A. George Nurser, D. Salas y Mélia, J. B. Palter, B. L. Samuels, J. Schröter, F. U.
 722 Schwarzkopf, D. Sidorenko, A. M. Treguier, Y.-h. Tseng, H. Tsujino, P. Uotila, S. Val-
 723 cke, A. Voltaire, Q. Wang, M. Winton, and X. Zhang (2014), An assessment of global
 724 and regional sea level for years 1993–2007 in a suite of interannual CORE-II simula-
 725 tions, *Ocean Modelling*, *78*, 35–89, doi:10.1016/j.ocemod.2014.03.004.
- 726 Griffies, S. M., G. Danabasoglu, P. J. Durack, A. J. Adcroft, V. Balaji, C. W. Böning, E. P.
 727 Chassignet, E. Curchitser, J. Deshayes, H. Drange, B. Fox-Kemper, P. J. Gleckler, J. M.
 728 Gregory, H. Haak, R. W. Hallberg, P. Heimbach, H. T. Hewitt, D. M. Holland, T. Ily-
 729 ina, J. H. Jungclaus, Y. Komuro, J. P. Krasting, W. G. Large, S. J. Marsland, S. Masina,
 730 T. J. McDougall, A. J. G. Nurser, J. C. Orr, A. Pirani, F. Qiao, R. J. Stouffer, K. E. Tay-
 731 lor, A. M. Treguier, H. Tsujino, P. Uotila, M. Valdivieso, Q. Wang, M. Winton, and
 732 S. G. Yeager (2016), Omip contribution to cmip6: experimental and diagnostic protocol
 733 for the physical component of the ocean model intercomparison project, *Geoscientific*
 734 *Model Development*, *9*(9), 3231–3296, doi:10.5194/gmd-9-3231-2016.
- 735 Hare, S. R., and N. J. Mantua (2000), Empirical evidence for north pacific regime shifts
 736 in 1977 and 1989, *Progress in Oceanography*, *47*(2), 103 – 145, doi:https://doi.org/10.

- 1016/S0079-6611(00)00033-1.
- Hoffman, M. J., M. Peregó, S. F. Price, W. H. Lipscomb, D. Jacobsen, I. Tezaur, A. G. Salinger, R. Tuminaro, and T. Zhang (2018), MPAS-Albany Land Ice (MALI): A variable resolution ice sheet model for Earth system modeling using Voronoi grids, *Geoscientific Model Development*, pp. 1–47, doi:10.5194/gmd-2018-78.
- Holland, M. M., D. A. Bailey, B. P. Briegleb, B. Light, and E. Hunke (2012), Improved Sea Ice Shortwave Radiation Physics in CCSM4: The Impact of Melt Ponds and Aerosols on Arctic Sea Ice, *Journal of Climate*, 25(5), 1413–1430, doi:10.1175/JCLI-D-11-00078.1.
- Holte, J., L. D. Talley, J. Gilson, and D. Roemmich (2017), An argo mixed layer climatology and database, *Geophysical Research Letters*, 44(11), 5618–5626, doi:10.1002/2017GL073426, 2017GL073426.
- Hunke, E. C., and J. K. Dukowicz (1997), An Elastic-Viscous-Plastic Model for Sea Ice Dynamics, *Journal of Physical Oceanography*, 27(9), 1849–1867, doi:10.1175/1520-0485(1997)027<1849:AEVPMF>2.0.CO;2.
- Hunke, E. C., and J. K. Dukowicz (2002), The Elastic-Viscous-Plastic Sea Ice Dynamics Model in General Orthogonal Curvilinear Coordinates on a Sphere – Incorporation of Metric Terms, *Monthly Weather Review*, 130(7), 1848–1865, doi:10.1175/1520-0493(2002)130<1848:TEVPSI>2.0.CO;2.
- Hunke, E. C., D. A. Hebert, and O. Lecomte (2013), Level-ice melt ponds in the Los Alamos sea ice model, CICE, *Ocean Modelling*, 71, 26–42, doi:10.1016/j.ocemod.2012.11.008.
- Hunke, E. C., W. H. Lipscomb, A. K. Turner, N. Jeffery, and S. Elliott (2015), CICE: the Los Alamos Sea Ice Model Documentation and Software User’s Manual Version 5.1, *Tech. rep.*, Los Alamos National Laboratory.
- Hurrell, J. W., J. J. Hack, D. Shea, J. M. Caron, and J. Rosinski (2008), A New Sea Surface Temperature and Sea Ice Boundary Dataset for the Community Atmosphere Model, *Journal of Climate*, 21(19), 5145–5153, doi:10.1175/2008JCLI2292.1.
- Jacobsen, D. W., M. Gunzburger, T. Ringler, J. Burkardt, and J. Peterson (2013), Parallel algorithms for planar and spherical Delaunay construction with an application to centroidal Voronoi tessellations, *Geosci. Model Dev.*, 6(4), 1353–1365, doi:10.5194/gmd-6-1353-2013.
- Johns, W. E., T. L. Townsend, D. M. Fratantoni, and W. D. Wilson (2002), On the Atlantic inflow to the Caribbean Sea, *Deep Sea Research Part I: Oceanographic Research Papers*, 49(2), 211–243, doi:10.1016/S0967-0637(01)00041-3.
- Killworth, P. D. (1983), Deep convection in the World Ocean, *Reviews of Geophysics*, 21(1), 1–26, doi:10.1029/RG021i001p00001.
- Kirtman, B. P., C. Bitz, F. Bryan, W. Collins, J. Dennis, N. Hearn, J. L. Kinter, R. Loft, C. Rousset, L. Siqueira, et al. (2012), Impact of ocean model resolution on ccsm climate simulations, *Climate dynamics*, 39(6), 1303–1328.
- Large, W., and S. Yeager (2009), The global climatology of an interannually varying air-sea flux data set, *Climate Dyn.*, 33(2-3), 341–364, doi:10.1007/s00382-008-0441-3.
- Large, W. G., J. C. McWilliams, and S. C. Doney (1994), Oceanic Vertical Mixing - a Review and a Model with a Nonlocal Boundary-Layer Parameterization, *Rev. Geophys.*, 32(4), 363–403.
- Laurindo, L. C., A. J. Mariano, and R. Lumpkin (2017), An improved near-surface velocity climatology for the global ocean from drifter observations, *Deep Sea Research Part I: Oceanographic Research Papers*, 124, 73–92.
- Lipscomb, W. H. (2001), Remapping the thickness distribution in sea ice models, *Journal of Geophysical Research: Oceans*, 106(C7), 13,989–14,000, doi:10.1029/2000JC000518.
- Lipscomb, W. H., and E. C. Hunke (2004), Modeling Sea Ice Transport Using Incremental Remapping, *Monthly Weather Review*, 132(6), 1341–1354, doi:10.1175/1520-0493(2004)132<1341:MSITUI>2.0.CO;2.

- 790 Lipscomb, W. H., and T. D. Ringler (2005), An Incremental Remapping Transport Scheme
791 on a Spherical Geodesic Grid, *Monthly Weather Review*, *133*(8), 2335–2350, doi:10.
792 1175/MWR2983.1.
- 793 Lipscomb, W. H., E. C. Hunke, W. Maslowski, and J. Jakacki (2007), Ridging, strength,
794 and stability in high-resolution sea ice models, *Journal of Geophysical Research:
795 Oceans*, *112*(C3), doi:10.1029/2005JC003355, C03S91.
- 796 Maltrud, M. E., and J. L. McClean (2005), An eddy resolving global 1/10° ocean simula-
797 tion, *Ocean Modelling*, *8*(1), 31–54, doi:10.1016/j.ocemod.2003.12.001.
- 798 Moore, J. K., S. C. Doney, and K. Lindsay (2004), Upper ocean ecosystem dynamics and
799 iron cycling in a global three-dimensional model, *Global Biogeochem. Cycles*, *18*(4),
800 GB4028, doi:10.1029/2004GB002220.
- 801 Moore, J. K., K. Lindsay, S. C. Doney, M. C. Long, and K. Misumi (2013), Marine
802 ecosystem dynamics and biogeochemical cycling in the Community Earth System
803 Model [CESM1(BGC)]: Comparison of the 1990s with the 2090s under the RCP4.5
804 and RCP8.5 scenarios, *J. Climate*, *26*(23), 9291–9312, doi:10.1175/JCLI-D-12-00566.1.
- 805 Nowlin, W. D., and J. M. Klinck (1986), The physics of the Antarctic Circumpolar Cur-
806 rent, *Reviews of Geophysics*, *24*(3), 469–491, doi:10.1029/RG024i003p00469.
- 807 Parkinson, C. L., and D. J. Cavalieri (2012), Antarctic sea ice variability and trends, 1979-
808 2010, *The Cryosphere*, *6*(4), 871–880, doi:10.5194/tc-6-871-2012.
- 809 Parkinson, C. L., D. J. Cavalieri, P. Gloersen, H. J. Zwally, and J. C. Comiso (1999), Arc-
810 tic sea ice extents, areas, and trends, 1978–1996, *Journal of Geophysical Research:
811 Oceans*, *104*(C9), 20,837–20,856, doi:10.1029/1999JC900082.
- 812 Petersen, M. R., D. W. Jacobsen, T. D. Ringler, M. W. Hecht, and M. E. Maltrud (2015),
813 Evaluation of the arbitrary Lagrangian–Eulerian vertical coordinate method in the
814 MPAS-Ocean model, *Ocean Modelling*, *86*, 93–113, doi:10.1016/j.ocemod.2014.12.004.
- 815 Prinsenber, S. J., and J. Hamilton (2005), Monitoring the volume, freshwater and heat
816 fluxes passing through Lancaster sound in the Canadian arctic archipelago, *Atmosphere-
817 Ocean*, *43*(1), 1–22, doi:10.3137/ao.430101.
- 818 Rauscher, S. A., T. D. Ringler, W. C. Skamarock, and A. A. Mirin (2012), Exploring a
819 Global Multiresolution Modeling Approach Using Aquaplanet Simulations, *Journal of
820 Climate*, *26*(8), 2432–2452, doi:10.1175/JCLI-D-12-00154.1.
- 821 Reckinger, S. M., M. R. Petersen, and S. J. Reckinger (2015), A study of overflow simu-
822 lations using MPAS-Ocean: Vertical grids, resolution, and viscosity, *Ocean Modelling*,
823 *96*, 291–313, doi:10.1016/j.ocemod.2015.09.006.
- 824 Redi, M. H. (1982), Oceanic isopycnal mixing by coordinate rotation, *Journal of Physical
825 Oceanography*, *12*(10), 1154–1158, doi:10.1175/1520-0485(1982)012<1154:OIMBCR>
826 2.0.CO;2.
- 827 Ringler, T., and P. Gent (2011), An eddy closure for potential vorticity, *Ocean Modelling*,
828 *39*(1), 125 – 134, doi:https://doi.org/10.1016/j.ocemod.2011.02.003, modelling and Un-
829 derstanding the Ocean Mesoscale and Submesoscale.
- 830 Ringler, T., M. Petersen, R. L. Higdon, D. Jacobsen, P. W. Jones, and M. Maltrud (2013),
831 A multi-resolution approach to global ocean modeling, *Ocean Modelling*, *69*, 211–232,
832 doi:10.1016/j.ocemod.2013.04.010.
- 833 Ringler, T., J. A. Saenz, P. J. Wolfram, and L. V. Roedel (2017), A thickness-weighted av-
834 erage perspective of force balance in an idealized circumpolar current, *Journal of Physi-
835 cal Oceanography*, *47*(2), 285–302, doi:10.1175/JPO-D-16-0096.1.
- 836 Ringler, T. D., J. Thuburn, J. B. Klemp, and W. C. Skamarock (2010), A unified approach
837 to energy conservation and potential vorticity dynamics for arbitrarily-structured C-
838 grids, *Journal of Computational Physics*, *229*(9), 3065–3090, doi:10.1016/j.jcp.2009.
839 12.007.
- 840 Ringler, T. D., D. Jacobsen, M. Gunzburger, L. Ju, M. Duda, and W. Skamarock (2011),
841 Exploring a Multiresolution Modeling Approach within the Shallow-Water Equations,
842 *Monthly Weather Review*, *139*(11), 3348–3368, doi:10.1175/MWR-D-10-05049.1.

- 843 Roach, A. T., K. Aagaard, C. H. Pease, S. A. Salo, T. Weingartner, V. Pavlov, and M. Ku-
844 lakov (1995), Direct measurements of transport and water properties through the
845 Bering Strait, *Journal of Geophysical Research: Oceans*, 100(C9), 18,443–18,457, doi:
846 10.1029/95JC01673.
- 847 Roemmich, D. (1981), Circulation of the Caribbean Sea: A well-resolved inverse prob-
848 lem, *Journal of Geophysical Research: Oceans*, 86(C9), 7993–8005, doi:10.1029/
849 JC086iC09p07993.
- 850 Saenz, J. A., Q. Chen, and T. Ringler (2015), Prognostic residual mean flow in an ocean
851 general circulation model and its relation to prognostic Eulerian mean flow, *J. Phys.*
852 *Oceanogr.*, 45(9), 2247–2260, doi:10.1175/JPO-D-15-0024.1.
- 853 Schauer, U., E. Fahrbach, S. Osterhus, and G. Rohardt (2004), Arctic warming through the
854 Fram Strait: Oceanic heat transport from 3 years of measurements, *Journal of Geophysi-*
855 *cal Research: Oceans*, 109(C6), C06,026, doi:10.1029/2003JC001823.
- 856 Schweiger, A., R. Lindsay, J. Zhang, M. Steele, H. Stern, and R. Kwok (2011a), Uncer-
857 tainty in modeled Arctic sea ice volume, *Journal of Geophysical Research: Oceans*,
858 116(C8), doi:10.1029/2011JC007084, C00D06.
- 859 Schweiger, A., R. Lindsay, J. Zhang, M. Steele, H. Stern, and R. Kwok (2011b), Uncer-
860 tainty in modeled arctic sea ice volume, *Journal of Geophysical Research: Oceans*,
861 116(C8), doi:10.1029/2011JC007084.
- 862 Sein, D. V., N. V. Koldunov, S. Danilov, Q. Wang, D. Sidorenko, I. Fast, T. Rackow,
863 W. Cabos, and T. Jung (2017), Ocean modeling on a mesh with resolution following the
864 local rossby radius, *Journal of Advances in Modeling Earth Systems*, 9(7), 2601–2614,
865 doi:10.1002/2017MS001099.
- 866 Skamarock, W. C., and A. Gassmann (2011), Conservative transport schemes for spherical
867 geodesic grids: High-order flux operators for ODE-based time integration, *Mon. Wea.*
868 *Rev.*, 139, 2962–2975, doi:10.1175/MWR-D-10-05056.1.
- 869 Skamarock, W. C., J. B. Klemp, M. G. Duda, L. D. Fowler, S.-H. Park, and T. D. Ringler
870 (2012), A Multiscale Nonhydrostatic Atmospheric Model Using Centroidal Voronoi
871 Tessellations and C-Grid Staggering, *Monthly Weather Review*, 140(9), 3090–3105, doi:
872 10.1175/MWR-D-11-00215.1.
- 873 Smith, R., P. Jones, B. Briegleb, F. Bryan, G. Danabasoglu, J. Dennis, J. Dukowicz,
874 C. Eden, B. Fox-Kemper, P. Gent, M. Hecht, S. Jayne, M. Jochum, W. Large, K. Lind-
875 say, M. Maltrud, N. Norton, S. Peacock, M. Vertenstein, and S. Yeager (2010), The Par-
876 allel Ocean Program (POP) reference manual: Ocean component of the Community
877 Climate System Model (CCSM), *Tech. rep.*, Los Alamos National Laboratory.
- 878 Sprintall, J., S. E. Wijffels, R. Molcard, and I. Jaya (2009), Direct estimates of the Indone-
879 sian Throughflow entering the Indian Ocean: 2004–2006, *Journal of Geophysical Re-*
880 *search: Oceans*, 114(C7), C07,001, doi:10.1029/2008JC005257.
- 881 Steele, M., R. Morley, and W. Ermold (2001), Phc: A global ocean hydrography with a
882 high-quality arctic ocean, *J. Climate*, 14(9), 2079–2087, doi:10.1175/1520-0442(2001)
883 014<2079:PAGOHW>2.0.CO;2.
- 884 Stewart, K. D., T. W. N. Haine, A. McC. Hogg, and F. Roquet (2017), On cabbeling and
885 thermobaricity in the surface mixed layer, *Journal of Physical Oceanography*, 47(7),
886 1775–1787, doi:10.1175/JPO-D-17-0025.1.
- 887 Stocker, T. F., D. Qin, G.-K. Plattner, M. Tignor, S. K. Allen, J. Boschung, A. Nauels,
888 Y. Xia, V. Bex, and P. M. Midgley (2013), Climate change 2013: The physical science
889 basis, *Tech. rep.*, doi:10.1017/CBO9781107415324, 1535 pp.
- 890 Thuburn, J., T. D. Ringler, W. C. Skamarock, and J. B. Klemp (2009), Numerical repre-
891 sentation of geostrophic modes on arbitrarily structured C-grids, *Journal of Computa-*
892 *tional Physics*, 228(22), 8321–8335, doi:10.1016/j.jcp.2009.08.006.
- 893 Trenberth, K. E., and J. M. Caron (2001), Estimates of meridional atmosphere and ocean
894 heat transports, *Journal of Climate*, 14(16), 3433–3443, doi:10.1175/1520-0442(2001)
895 014<3433:EOMAAO>2.0.CO;2.

- 896 Turner, A. K., and E. C. Hunke (2015), Impacts of a mushy-layer thermodynamic ap-
 897 proach in global sea-ice simulations using the CICE sea-ice model, *Journal of Geophys-*
 898 *ical Research: Oceans*, 120(2), 1253–1275, doi:10.1002/2014JC010358.
- 899 Turner, A. K., E. C. Hunke, and C. M. Bitz (2013), Two modes of sea-ice gravity
 900 drainage: A parameterization for large-scale modeling, *Journal of Geophysical Research:*
 901 *Oceans*, 118(5), 2279–2294, doi:10.1002/jgrc.20171.
- 902 van der Werf, P. M., P. J. van Leeuwen, H. Ridderinkhof, and W. P. M. de Ruijter (2010),
 903 Comparison between observations and models of the Mozambique Channel trans-
 904 port: Seasonal cycle and eddy frequencies, *Journal of Geophysical Research: Oceans*,
 905 115(C2), C02,002, doi:10.1029/2009JC005633.
- 906 Whitworth, T., and R. G. Peterson (1985), Volume Transport of the Antarctic Circumpolar
 907 Current from Bottom Pressure Measurements, *J. Phys. Oceanogr.*, 15(6), 810–816, doi:
 908 10.1175/1520-0485(1985)015<0810:VTOTAC>2.0.CO;2.
- 909 Wolfram, P. J., and T. D. Ringler (2017a), Quantifying residual, eddy, and mean flow ef-
 910 fects on mixing in an idealized circumpolar current, *J. Phys. Oceanogr.*, 47(8), 1897–
 911 1920, doi:10.1175/JPO-D-16-0101.1.
- 912 Wolfram, P. J., and T. D. Ringler (2017b), Computing eddy-driven effective diffusivity
 913 using Lagrangian particles, *Ocean Modell.*, 118, 94–106, doi:10.1016/j.ocemod.2017.08.
 914 008.
- 915 Wolfram, P. J., T. D. Ringler, M. E. Maltrud, D. W. Jacobsen, and M. R. Petersen (2015),
 916 Diagnosing isopycnal diffusivity in an eddying, idealized midlatitude ocean basin via
 917 Lagrangian, In-situ, Global, High-Performance Particle Tracking (LIGHT), *J. Phys.*
 918 *Oceanogr.*, 45(8), 2114–2133, doi:10.1175/JPO-D-14-0260.1.
- 919 Woodring, J., M. Petersen, A. Schmeiß er, J. Patchett, J. Ahrens, and H. Hagen (2016),
 920 In Situ Eddy Analysis in a High-Resolution Ocean Climate Model, *IEEE Transactions*
 921 *on Visualization and Computer Graphics*, 22(1), 857–866, doi:10.1109/TVCG.2015.
 922 2467411.
- 923 Zwally, H. J., J. C. Comiso, C. L. Parkinson, D. J. Cavalieri, and P. Gloersen (2002),
 924 Variability of Antarctic sea ice 1979–1998, *Journal of Geophysical Research: Oceans*,
 925 107(C5), 9–1–9–19, doi:10.1029/2000JC000733.